REPORT DOCUMENTATION PAGE

Form Approved
OMB No. 0704-0188

PLEASE DO NOT RETURN YOUR FORM TO THE ABOVE ORGANIZATION.

1. REPORT DATE *(DD-MM-YYYY)*	2. REPORT TYPE	3. DATES COVERED *(From - To)*
22-09-2010	Final	06/01/2008-12/31/2009

4. TITLE AND SUBTITLE
Flight Experiments on swept-wing roughness receptivity. Validation data for modeling and computations

5a. CONTRACT NUMBER
C08-00844

5b. GRANT NUMBER
FA9550-08-1-0475

5c. PROGRAM ELEMENT NUMBER

6. AUTHOR(S)
William S. Saric

5d. PROJECT NUMBER
32525-A2960

5e. TASK NUMBER
AFOSR FA9550-08-1-0475 Final Report

5f. WORK UNIT NUMBER

7. PERFORMING ORGANIZATION NAME(S) AND ADDRESS(ES)
Texas Engineering Experiment Station
3000 TAMUS
College Station, TX 77843-3000

8. PERFORMING ORGANIZATION REPORT NUMBER

9. SPONSORING/MONITORING AGENCY NAME(S) AND ADDRESS(ES)
Air Force Office of Scientific Research
875 North Randolph Suite 325, Room 3112
Arlington, Virginia 22203

10. SPONSOR/MONITOR'S ACRONYM(S)
AFOSR

11. SPONSOR/MONITOR'S REPORT NUMBER(S)
AFRL-OSR-VA-TR-2012-0292

12. DISTRIBUTION/AVAILABILITY STATEMENT

DISTRIBUTION A: Approved for Public Release

13. SUPPLEMENTARY NOTES

14. ABSTRACT

Micron-sized, spanwise-periodic Discrete Roughness Elements (DREs) were applied to the leading edge of a 30-degree swept-wing. The test article was attached vertically to the port wing of a Cessna O-2A aircraft and operated at a chord Reynolds number of 6.5 to 7.5 million. With a polished leading edge, 80% laminar flow was observed corresponding to N-factors greater than 12. Critically spaced DREs were applied at the leading edge to excite the crossflow instability and move transition forward. In this case, calibrated, multi-element hotfilm sensors were used to measure disturbance wall shear stress. The roughness height was varied from 0 to 50 microns both in the positive (bumps) and negative (dimples) sense. Thus, the disturbance amplitude variations were determined as a function of modulated DRE heights.

15. SUBJECT TERMS
swept-wing roughness receptivity

16. SECURITY CLASSIFICATION OF:			17. LIMITATION OF ABSTRACT	18. NUMBER OF PAGES	19a. NAME OF RESPONSIBLE PERSON
a. REPORT	b. ABSTRACT	c. THIS PAGE			William Saric
U	U	U	UU	33	19b. TELEPHONE NUMBER *(Include area code)* 979-862-1749

Reset

FLIGHT EXPERIMENTS ON SWEPT-WING ROUGHNESS RECEIPTIVITY. VALIDATION DATA FOR MODELING AND COMPUTATIONS

AFOSR GRANT FA9550-08-1-0475
FINAL TECHNICAL REPORT

William S. Saric
Aerospace Engineering Department
Texas A&M University
College Station, Texas 77843-6051

ABSTRACT

Micron-sized, spanwise-periodic Discrete Roughness Elements (DREs) were applied to the leading edge of a 30-degree swept-wing. The test article was attached vertically to the port wing of a Cessna O-2A aircraft and operated at a chord Reynolds number of 6.5 to 7.5 million. With a polished leading edge, 80% laminar flow was observed corresponding to N-factors greater than 12. Critically spaced DREs were applied at the leading edge to excite the crossflow instability and move transition forward. In this case, calibrated, multi-element hotfilm sensors were used to measure disturbance wall shear stress. The roughness height was varied from 0 to 50 microns both in the positive (bumps) and negative (dimples) sense. Thus, the disturbance amplitude variations were determined as a function of modulated DRE heights.

Nomenclature

Re_c	=	chord Reynolds number
Λ_{LE}	=	leading edge sweep
α	=	aircraft angle of attack
β	=	aircraft sideslip angle
AoA	=	SWIFT model angle of attack
λ_{crit}	=	most unstable stationary crossflow vortex spacing
Re_{trans}	=	Reynolds number at transition
k	=	roughness height
Re_k	=	Reynolds number based on roughness height
u_k	=	absolute velocity at the roughness height
ν_k	=	kinematic viscosity at the roughness height
k/δ	=	ratio of roughness height to boundary-layer height
δ	=	boundary-layer height when u = 0.99U_∞
d	=	roughness diameter
d/λ	=	ratio of roughness diameter to roughness spacing
τ_w	=	wall shear stress
Δp	=	difference between Preston tube pressure and local static pressure
d_{Prest}	=	outer diameter of Preston tube
ρ	=	freestream density
ν	=	freestream kinematic viscosity
$KTAS$	=	true airspeed in knots
E_o	=	hotfilm voltage with zero shear stress
E	=	hotfilm voltage
$E_{measured}$	=	measured hotfilm voltage
T_{nom}	=	nominal temperature used for temperature compensation
ST	=	surface temperature next to the hotfilm
m	=	temperature drift for hotfilm
c_f	=	skin- friction coefficient

I. Introduction

This paper describes a series of flight tests conducted at the Texas A&M Flight Research Laboratory (FRL) to study the effects of micron-sized, spanwise-periodic, Discrete Roughness Elements (DREs) on a 30-degree swept-wing. A 240 lb swept-wing test article was mounted vertically to the port pylon of a Cessna O-2A aircraft. The test article was operated at a chord Reynolds number, Re_c, of 6.5 to 7.5 million to match the flight conditions for the *Sensorcraft* aircraft. The overall mission objectives were to perform Laminar Flow Control (LFC) on the test article with the use of DREs. However, the focus of the current set of experiments, and this paper, is to understand the receptivity mechanism due to the introduction of artificial roughness near the leading edge of the model. The test article is described here as the Swept-Wing In-Flight Testing model or SWIFT model.

It is well understood that range and endurance are strongly dependent on the aircraft Lift over Drag ratio, *L/D*. Range and endurance scale proportionally to *L/D*. Improvements in lift can be made, but one of the most promising improvements in *L/D* is achieved by reducing the drag[1]. Laminar flow on the wings, empennage, and parts of the fuselage is the most promising technology for reducing the overall drag on a flight vehicle. Laminar flow has been a goal for aerodynamicists and aircraft designers for decades, but has only been incorporated into a few designs. Above and beyond the increase in range and endurance, a laminar-flow wing will produce less drag, decreasing the required engine thrust, resulting in less fuel burn and less engine noise. With the cyclical nature of high fuel prices, both Sensorcraft and every aerodynamic vehicle can benefit from laminar flow technology.

The targeted Re_c for the notional aircraft is 6.5 to 7.5 million under flight conditions of Mach 0.6 at 60,000 ft. The leading edge sweep, Λ_{LE}, of the vehicle is 30°. Beyond approximately 15° to 20° of Λ_{LE}, a wing is subject to crossflow that cannot be stabilized by a favorable pressure gradient. It is this class of airfoils that the experiments address: a wing subcritical to viscous 2-D instabilities, but destabilized by 3-D crossflow. This series of flight experiments is a successor to approximately 15 years of research focusing on laminar-flow swept-wings with the use of DREs. Promising results have been achieved[2] at low speeds in a low-turbulence wind tunnel with the use of DREs on a 45° swept-wing. Subcritical roughness was placed at the neutral point, or point of initial disturbance growth, of the swept-wing and transition was delayed beyond the naturally occurring location. These experiments[2] were limited to a Re_c of 3.5 million for a 1.83 m chord model at 30 m/s. This technique was then applied to a 30-degree swept-wing model operating at Mach 1.85 on an F-15 aircraft at NASA Dryden[3]. A Re_c of 10 million was achieved in these experiments. Almost full chord laminar flow was achieved on the lower part of the model at Mach 1.85 and Mach 0.91, despite being faced with a spanwise flow variation across the model generated by the fuselage of the F-15 aircraft[3].

A. Crossflow Dominated Transition

There are several instabilities that can lead to boundary-layer transition on a swept-wing. These include streamwise viscous instabilities such as Tollmien-Schlichting (T-S) waves, centrifugal instabilities, attachment-line contamination, and crossflow vortices. A recent review of the instabilities on a swept-wing can be found in Ref. 4. The pressure distribution on the SWIFT model has been tailored to stabilize the T-S waves by incorporating an aft pressure minimum at 70% *x/c*. Centrifugal instabilities, such as Görtler vortices, are avoided because concave curvature has been avoided near the leading edge. Attachment-line contamination has been avoided by designing the SWIFT model with a free end, not attached to any turbulent boundary layers. These design features isolate the remaining crossflow instability which is destabilized by the favorable pressure gradient used to stabilize the TS waves. This leads to a category of LFC titled Swept-Wing Laminar Flow Control (SWLFC). SWLFC takes into account all the features of Natural Laminar Flow (NLF) with a slight favorable pressure gradient, but incorporates distributed roughness at the leading edge for added control of the unstable crossflow vortices. It is this class of LFC that was studied in the SWIFT flight test program described here.

It is well understood that the pressure gradient combined with the curved streamlines on the swept-wing produce a crossflow boundary layer. The crossflow component, approximately normal to the local inviscid streamline, has an inflection point which has been proven to be unstable in the inviscid limit. The crossflow instability manifests itself as growth in the form of co-rotating vortices, where low-momentum fluid at the surface is drawn up higher in the boundary layer, while higher momentum fluid is entrained lower in the boundary layer. This produces co-rotating stationary crossflow vortices forming around the crossflow inflection point that ultimately leads to and feeds into the

high-frequency secondary instability resulting in eventual breakdown to turbulence. Reference 5 gives a thorough review of the development and breakdown of 3-D boundary layers. Figure 1 has experimental data showing the streamwise growth of crossflow vortices taken from boundary layers scans in the experiments[6]. For this case, DREs were applied at the leading edge to generate uniform crossflow vortices spaced 12 mm apart (parallel to the leading edge).

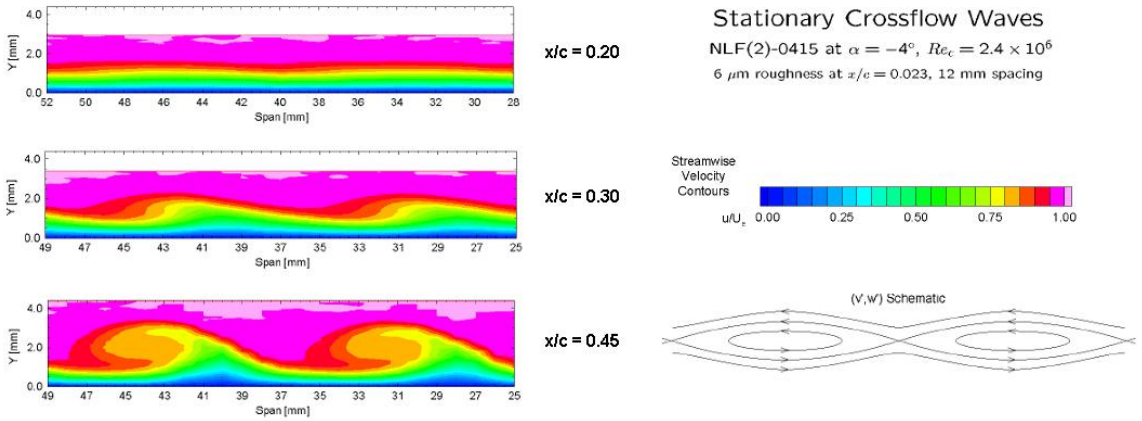

Figure 1: Development of stationary crossflow waves in the chordwise direction. Figure adapted from Ref. 6.

On a swept wing, designed to be subcritical to TS waves, the stationary crossflow vortices will grow linearly, modify the mean-flow boundary layer, producing accelerated, decelerated, and doubly inflectional boundary layer profiles[6]. These modified profiles then feed into the high-frequency, secondary instability, where breakdown to transition occurs on a much faster convective time scale[7,8]. The spacing of the stationary crossflow vortices can be predicted well by Linear Stability Theory (LST). The most unstable wave, i.e. the one exhibiting the highest disturbance growth, will dominate and will be observed in well-controlled swept-wing experiments.

When studying boundary-layer transition on the swept-wing, the breakdown to turbulence can be divided into three categories. The first stage is receptivity where long-wavelength disturbances in the environment or surface imperfections produce short-wavelength disturbances in the boundary layer. Morkovin[9] is credited with the first explanation of the receptivity process. Once the initial disturbances are introduced through the receptivity mechanism, linear growth occurs in the form of crossflow vortices. LST predicts the growth rate in this linear region well. Lastly, the secondary instability dominates and transition to turbulence occurs very rapidly. When examining these three categories, most attention is spent investigating the linear growth region. The receptivity region is the least understood and very few experiments deal with this topic[10]. This paper describes a series of experiments focusing on the receptivity problem for the swept-wing. Specifically disturbance amplitudes were measured with calibrated, surface-mounted, multi-element hotfilms downstream of DREs with modulating heights.

II. Experimental Setup

A. Test Aircraft

A 1968 Cessna O-2A Skymaster was purchased specifically for the SWIFT experiments, and was dedicated to the program for the majority of the time period. The O-2A is a high-wing, twin-engine aircraft featuring the very distinctive twin tail and centerline thrust configuration. The O-2A is a military modification of the Cessna 337 and includes four wing-mounted pylons, reinforced spars for cyclic loading, observation windows on both the pilot and co-pilot sides, a third row radio rack in the cabin, and jettisonable cabin doors and pilot-side window in the case of an emergency evacuation. Of all the features incorporated into the O-2A design, the wing-mounted pylons were specifically targeted for mounting a large swept-wing test article.

B. SWIFT Model

The SWIFT model has a leading-edge sweep of Λ_{LE} = 30° and a chord of 54 inches (1.37 m) to provide the targeted Re_c between 6.5 and 7.5 million within the performance capabilities of the O-2A during a dive. The span of the SWIFT model was nominally 42 inches at the leading edge, but a 4 degree cut starting aft of the leading edge was incorporated into the design for added ground clearance during rotation at take-off and landing. The model has two interchangeable leading edges depending on the given flight test. Leading edge #1 was polished aluminum and has static pressure ports. This leading edge was used for all flying quality flights and pressure (*Cp*) measurements. Leading edge #2 was without pressure ports and was used for demonstrating the DRE technology and hotfilm receptivity experiments. Both leading-edge attachments have the same dimensions and were mounted to the rest of the airfoil at the 15% chord position. From 15% chord to the trailing edge, the surface had a black powder-coat layer which provided thermal insulation and a non-reflective surface for transition detection with an infrared camera. The interior cavity of the model was milled out to provide the lightest possible structure, but still strong enough to withstand the aerodynamic loads with a necessary factor of safety. All interior stiffeners were milled out of the design from a solid block of aluminum resulting in a model composed of three main parts; the test-side surface, the non test-side surface, and the leading edge. The three main parts were assembled with all bolts on the non-testside of the model, leaving the testside of the model disturbance free. Figure 2 shows the test aircraft with the SWIFT model mounted to the port wing and a hotwire sting mounted on the starboard wing.

Figure 2: Cessna O-2A aircraft with SWIFT model and hotwire sting

C. Freestream Measurements

An Aeroprobe, conical-tip, five-hole probe was used for all freestream measurements of total pressure, static pressure, aircraft angle of attack (α), and aircraft sideslip angle (β). The five-hole probe was 24 inches long and was mounted to the non-testside of the SWIFT model. A custom bracket was designed to extend the five-hole probe out into the freestream. The six pressure ports on the five-hole probe led to four Honeywell Sensotech FP2000 pressure transducers inside the internal cavity of the model. An Omega 100-ohm RTD was mounted underneath the port wing of the O-2A for total temperature measurements. The five-hole probe was always mounted to the SWIFT model to make localized measurements of the conditions upstream of the SWIFT model. Rhodes et al.[11] showed that there was a spanwise flow variation between the port wing and starboard wing, requiring localized measurements at the SWIFT model.

Freestream turbulence levels were recorded prior to flying with the SWIFT model. Recordings were made in both the level and dive attitude with 5 μm hotwires. During the test conditions, the turbulence levels were in a range between 0.05% and 0.07% of the freestream velocity. All hotwire signals were bandpassed between 1Hz and 10 kHz with a Kemo VBF44 bandpass filter[12].

A new coordinate system was developed for studying this unconventional, vertically-mounted airfoil. The aircraft angle of attack, α, corresponds to a change in sweep on the SWIFT model. An increase in α decreases Λ_{LE}. The aircraft sideslip angle β corresponds to the angle of attack on the SWIFT model. However, to preserve the convention for positive β, the SWIFT angle of attack is the opposite of β. Negative angles of attack on SWIFT correspond to positive β values. Because of the sometimes confusing nature of the symbols, β will always refer to aircraft sideslip, and where necessary the SWIFT angle of attack will be denoted as *AoA*. α will always be referenced as aircraft angle of attack, and changes in sweep on SWIFT will be denoted with Λ_{LE}. An attempt is made to use both conventions in some figures to hopefully eliminate confusion. Equations 1 and 2 show the relationship between the four variables of interest.

$$\Lambda_{LE} = 30^{\circ} - \alpha \tag{1}$$

$$AoA = -\beta \tag{2}$$

D. Instrumentation

During all flights the Flight Test Engineer (FTE) operated the instrumentation located on the third row instrumentation rack. The FTE operated a Dell Precision M65 laptop running Windows XP and Labview 8.2. A Magma 4-slot PCI–PCMCIA bridge provided the necessary interface between the PCI DAQboards used for data acquisition and the laptop PCMCIA card. Two Otek LPE panel meters were added to the pilot's instrumentation panel to monitor β and Re_c. β and Re_c were the two most important variables for these experiments, so the pilot was expected to maintain these two parameters while on test conditions during the dive.

For the receptivity measurements described in this paper, two AA Labs AN-1003, ten-channel, constant temperature anemometers (CTAs) were added to the cabin of the O-2A aircraft. A custom instrumentation rack was built and mounted aft of the pilot's seat to secure the CTAs. Due to the high weight of each anemometer (50 lbs each), the CTAs had to be mounted as far forward as possible to avoid aft CG problems. An Exeltech XP-600, pure sinewave, AC to DC inverter was installed to power all AC powered instruments. However, a Tripp Lite line conditioner was added to the power line of the CTAs to avoid any possible voltage spikes from the inverter and to reduce any electronic noise.

E. Safety Analysis

Prior to the first flight with the SWIFT model, an extensive safety analysis was performed on the model and critical components of the aircraft. The FRL team, Northrop Grumman, and the Air Force Research Laboratory all performed the necessary load estimations, stress analysis, flutter analysis, and low speed directional control analysis

before the first flight. Furthermore, three static load tests were performed, where flight hardware was loaded to 1.5 times the highest expected load. Thorough reviews of the analysis can be found in Refs. 13 and 14. Furthermore, a review of the flying qualities and flutter clearance flights is provided in Ref. 12.

III. *Cp* Measurements

The SWIFT program consisted of both a computational effort and an experimental effort. The experimental part is described here, whereas the computational effort is summarized in Rhodes et al.[12] where they developed a solid model of the aircraft with the SWIFT model and performed a full Navier-Stokes analysis on the entire flowfield. The primary objective of this computational analysis was to compare the *Cp* measurements recorded in flight with the calculated Navier-Stokes solution. Once these matched, within experimental error, then the computations proceeded to provide boundary-layer and stability calculations for the experiments. The primary objective for conducting experimental *Cp* measurements on the SWIFT model was to determine which *AoA*s produced sufficient crossflow, resulting in a crossflow-dominated transition. An accelerated boundary layer back to the pressure minimum at 70% chord was the desired test point for studying the effect of DREs on transition.

The SWIFT model contains 64 static pressure ports on the surface. The pressure scanner was a ±5 psid, 16-bit, Pressure Systems scanner. The scanner was imbedded inside the model to reduce pressure lag time within the tubing. For all *Cp* flights, the pressure scanner used the freestream static pressure from the five-hole probe as the reference pressure.

A. *Cp* Comparison with CFD

The pilot used both the real-time Re_c and β display during these measurements to maintain conditions as close as possible to the targeted values. During smooth atmospheric conditions the pilot could routinely hold β to within ± 0.1 degrees for a five-second pressure acquisition. For each test point, a five-second acquisition of freestream conditions and *Cp* values was recorded. These data were then averaged over the five seconds, but the scatter of *Cp* data were used to generate error bars to compare with the computations. The goal was to measure *Cp* values in the dive attitude at *AoA* values between -5 degrees and +2 degrees at 0.5 degree increments. Figure 3 shows *Cp* values for the root pressure port row for three representative *AoA* cases. Also displayed in the same figure are the coordinates of the SWIFT airfoil, with the suction side of the airfoil considered the test side of the model facing the cabin of the O-2A. This paper will only focus on the root pressure port row. The SWIFT model contains two rows of pressure port rows spaced 16 inches apart. However, the receptivity measurements described here are only conducted at the top, or root, pressure port row. Figure 4 shows the relationship between the two rows. The bottom half of the model was used for demonstrating the LFC strategy with the DREs, and is described in Ref. 15. As a result, only *Cp* data for the root pressure port row are presented here. Moreover, it was discovered that the first few static pressure ports produced turbulent wedges above a Re_c of 7.2 million. Therefore, all *Cp* measurements were made below this threshold to prevent turbulent wedges.

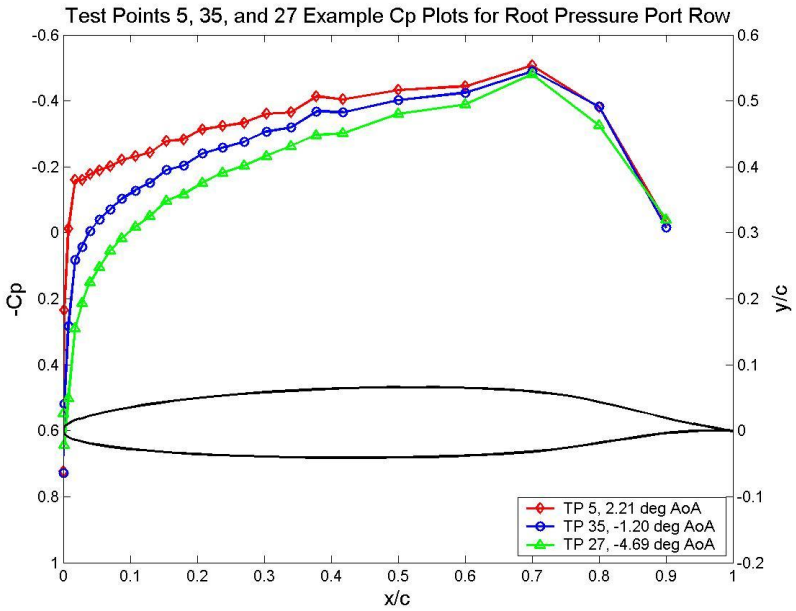

Figure 3: *Cp* data for three different test points at the root pressure port row

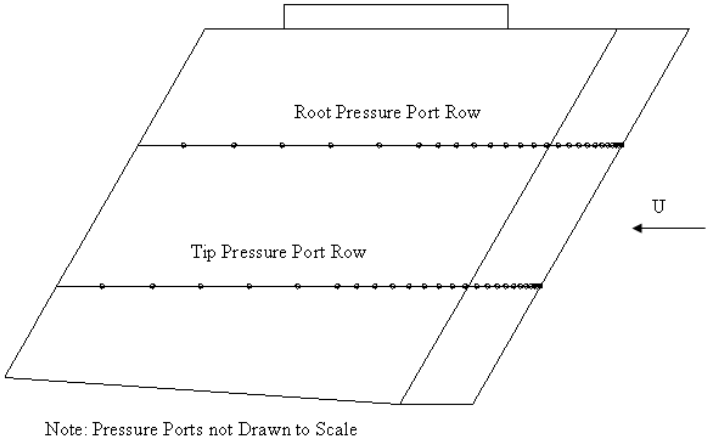

Figure 4: Schematic of SWIFT model showing both root and tip pressure port rows

The test points selected in Fig. 3 represent the highest, the middle, and one of the lowest *AoA* values tested during this campaign. Of the three conditions displayed in Fig. 3, most attention was paid to Test Point 27 at -4.69 degrees *AoA* because this test point generated sufficient amounts of crossflow. What is uniform about all three test points, and both pressure port rows, is that the pressure minimum is near 70% *x/c* at all *AoAs* tested, and all test points show an accelerated favorable pressure gradient back to this point. Overall the shape of each *Cp* curve was promising and expected based on the initial airfoil design.

This paper focuses on two *AoA* conditions for the receptivity measurements described later in Section VI. Figures 5 and 6 show a comparison between the experimental data, with error bars, and the calculated *Cp* distribution from Ref. 11. Figure 5 is at -2.61 deg *AoA* which demonstrated laminar flow back to 80% *x/c*. This condition proved to generate little crossflow growth, but was used to see if the crossflow instability could be excited with DREs spaced at the most unstable crossflow vortex spacing, λ_{crit}. Figure 6 at -4.69 deg *AoA* shows early transition and strong crossflow growth. Both Fig. 5 and Fig. 6 show good agreement between the experimental and calculated *Cp*.

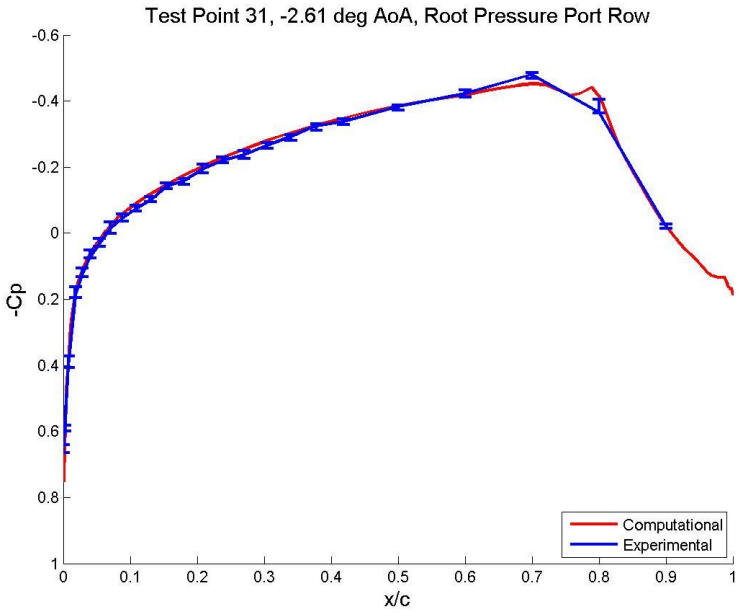

Figure 5: Experimental and computational comparison at -2.61 deg *AoA* for the root pressure port row

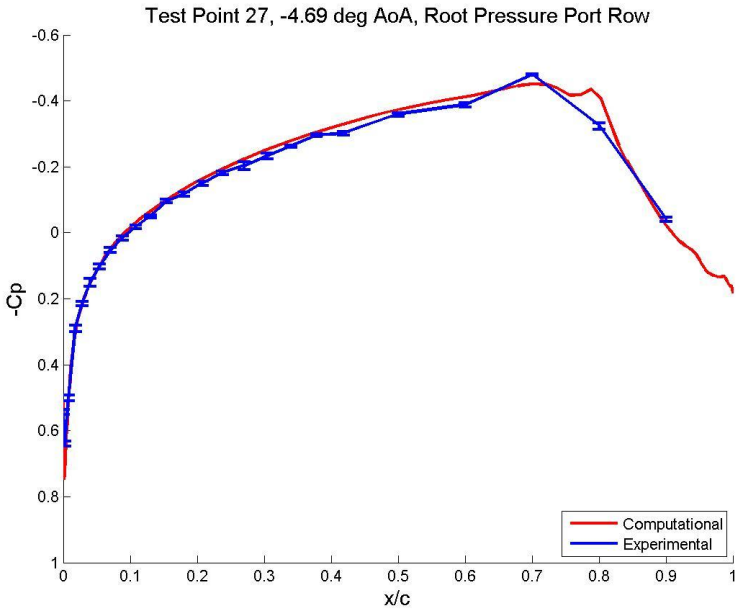

Figure 6: Experimental and computational comparison at -4.69 deg *AoA* for the root pressure port row

IV. Baseline Infrared Thermography

Infrared (IR) thermography was used to visualize boundary-layer transition on the SWIFT model. One advantage of using this technique is that no obtrusive probes or treatments are required on the surface of the model and only a non-reflective surface and a temperature differential between the laminar region and the turbulent region are required to visualize transition. The IR camera can record a global image of transition and hence has proven to be a valuable tool for transition detection. It has been used in the F-15 flight experiments at NASA Dryden[16], T-34C

experiments[17], and B737 experiments[18] with much success. The technique has been used here with both a polished leading edge and a painted leading edge to document changes in transition for different random roughness conditions at the leading edge. A large range of *AoAs* between -0.5 and -5.5 degrees has been tested here to get a broad sampling of the crossflow instability. There is little crossflow growth at the upper *AoA* end, and strong crossflow growth at the lower end.

A FLIR SC3000 camera was used for all IR flights. This camera operates in the 8-9 μm spectral range which is best suited for colder bodies. The SC3000 has a GaAs Quantum-Well Infrared Photodetector which is cooled to 70 K with an onboard Stirling motor cooler. The camera has a sensitivity of 0.02 °C at a temperature of 30 °C. However, a temperature difference of at least 0.3 °C between the laminar region and the turbulent region was necessary to clearly identify a transition pattern.

The temperature lapse rate in the atmosphere was used to generate the temperature differential between the freestream and the model surface. The model was first cold soaked at 10,500 feet until a uniform temperature was reached on the model. The FTE used the IR camera to decide when the model was at a uniform temperature, which typically took thirty minutes. As the model descended into warmer air, the turbulent region on the aft section of the model heated up faster than the laminar region due to the higher convective heat transfer rate and recovery factor in the turbulent boundary layer[19]. At the end of the dive it was possible to generate as much as a 3 ºC differential between the laminar and turbulent regions, which was well within the sensitivity of the SC3000 camera.

A. IR Thermography with the Polished Leading Edge

Transition data were first collected with leading edge #2 with a polished leading edge. The surface roughness was measured to be 0.33 μm rms with 2.20 μm average peak-to-peak values using a Mitutoyo SJ-400 surface roughness tester. Figure 7 shows a representative IR image for this leading edge at an *AoA* of -1.88 degrees. Note that the five-hole probe is not mounted to the SWIFT model in this image since it was recorded prior to adding the five-hole probe. The *AoA* measurements have been corrected to correspond to the values on the port wing, based on measurements made on the starboard wing.

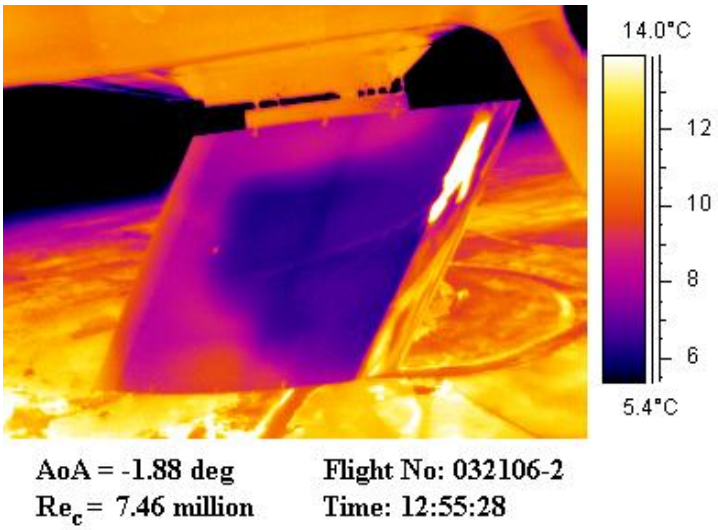

Figure 7: Baseline IR image with the polished leading edge at -1.88 degree *AoA*

Figure 7 shows transition at 80% *x/c* in the area of interest at half-span. The laminar region shows up as a colder temperature while the turbulent region beyond 80% *x/c* shows up warmer with the IR camera. The "warm" region near the top of the model is the IR reflection of the cabin Plexiglas windows. The thin bright line crossing mid-span is the IR diffraction from the bottom of the fuselage. The very bright area on the leading edge is the image of the forward engine and propeller. The tick marks at the top and bottom of the airfoil are at 40%, 60%, and 80% chord. With a polished leading edge, NLF was achieved beyond the pressure minimum at all test points with *AoAs* greater than -3 degrees. Transition was observed at 80% *x/c* which was much higher than anticipated. The highest N-factor

calculated for this *AoA* was 10 for a Re_c of 7.08 million. Other cases showed transition at 80% chord for N =12 at Re_c of 7.46 million and N =14 at Re_c of 8 million. These considerably high N-factors demonstrate the low freestream turbulence of flight. Because transition was observed beyond the pressure minimum, the instability for this case was probably T-S waves due to the adverse pressure gradient aft of 70% *x/c*. Despite calculating high N-factors, the transition results showed that the crossflow growth was weak with the polished leading edge and *AoA* values greater than -3 degrees. This is because transition was not observed forward of the pressure minimum. As a result, a design change was needed to destabilize the crossflow instability necessary for the receptivity measurements.

B. IR with a Painted Leading Edge

Leading edge #1 was painted to excite the crossflow instability and move transition forward of the 80% location. At this time in the flight program, the *Cp* measurements had been completed and there was good agreement between the computational and experimental *Cp* curves. Therefore, the *Cp* leading edge was painted with an epoxy primer and Jet Glow polyurethane paint with no thinning agent to purposely produce a rough surface. The static pressure ports were filled in with Bondo. A first round of paint with thinning agent proved to be ineffective at moving transition forward. Therefore, the second attempt at painting the leading edge was purposely geared towards producing an "orange peel" effect for an even rougher surface. As in the polished leading edge case, the surface roughness of the painted leading edge without the thinning agent was measured. The region forward of 2% *x/c* was sanded down with 1000 grit sand paper to provide a uniform base for future flights incorporating DREs. This section had an rms roughness of 1.66 μm, and average peak-to-peak values of 7.69 μm. The region from 2% *x/c* to 15% *x/c* was untouched after painting. This section had a higher surface roughness of 6.24 μm rms, with average peak-to-peak values of 31.42 μm.

Figures 8 through 11 show IR images with the painted leading edge under different *AoA* conditions. Note that the leading edge is now painted so detail in this region can be captured with the IR camera. Another addition in Figs. 8 through 11 is the five-hole probe extending forward of the leading edge. The images depicted in these four figures were recorded after adding the five-hole probe, so the *AoA* values did not require any correction.

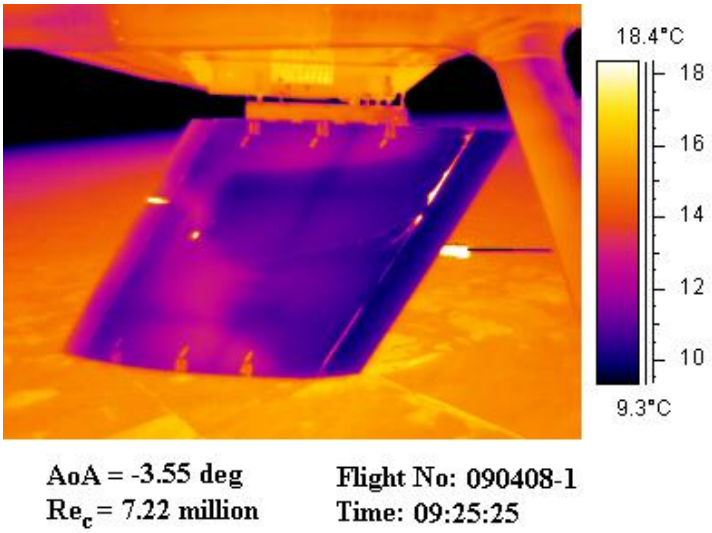

Figure 8: Baseline IR image with the painted leading edge at -3.55 degree *AoA*

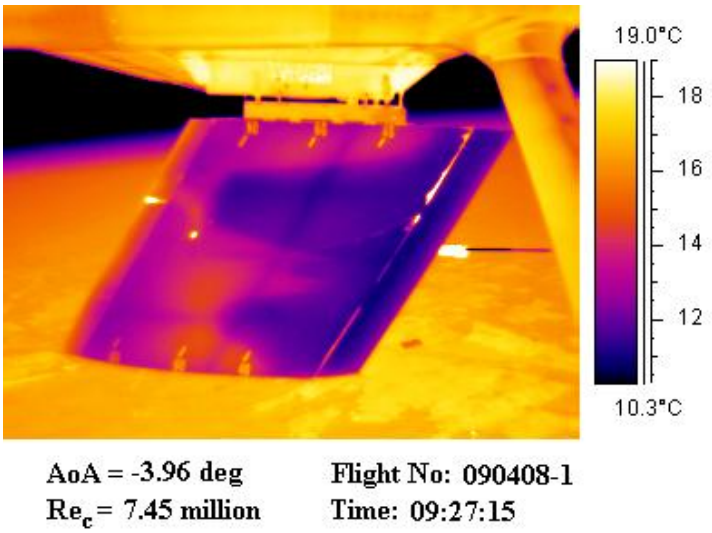

Figure 9: Baseline IR image with the painted leading edge at -3.96 degree *AoA*

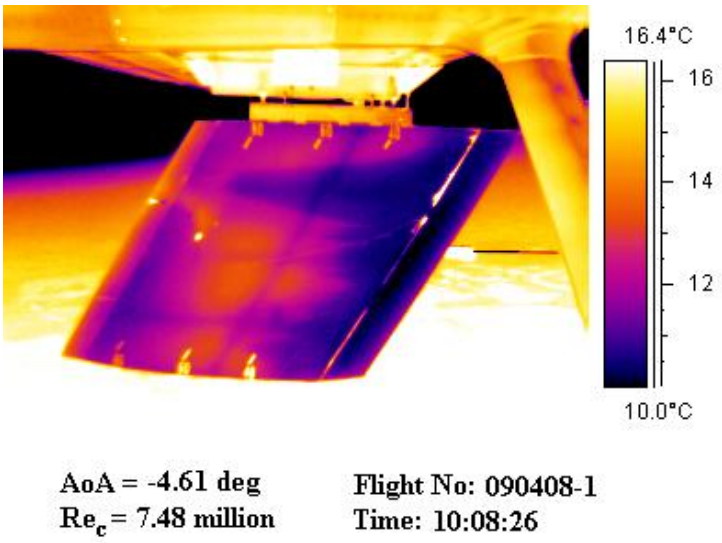

Figure 10: Baseline IR image with the painted leading edge at -4.61 degree *AoA*

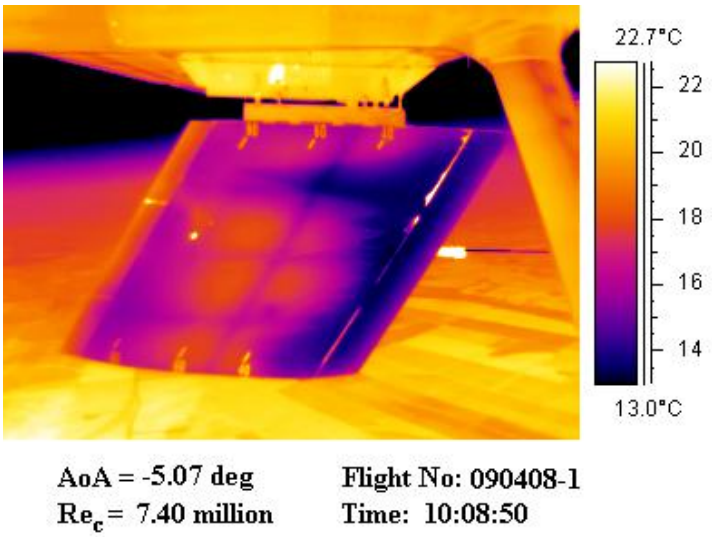

Figure 11: Baseline IR image with the painted leading edge at -5.07 degree *AoA*

Figures 8 through 11 show IR images with the painted leading edge between -3.55 degrees and -5.07 degrees *AoA*. At -3 degrees *AoA*, the model is laminar back to 80% *x/c*, much like the IR image depicted in Fig. 7. However, there is a big jump in transition location in Fig. 9 when the *AoA* is decreased to -3.96 degrees, which is not seen with the polished leading edge. This abrupt change in transition is due to the elevated crossflow instability with the painted leading edge. A decrease in *AoA* of less than half of a degree moved transition forward from 50% *x/c* to 30% *x/c*. As the *AoA* continues to decrease, there is no longer a large forward jump in the transition location like in Fig. 9, but a more gradual growth in spanwise turbulence. At -5.07 degrees *AoA*, the entire model starts to fill in with a turbulent transition front that creeps forward slightly to approximately 20% *x/c*. Another observation with the images in Figs. 8 through 11 is that the painted leading edge did very little to destabilize the regions above and below the root and tip pressure port rows, respectively. It is not until -5.07 degrees *AoA* that these two regions start to fill in and produce a uniform transition front at 20% *x/c*.

C. Baseline IR Comparison

A comparison between the polished and painted leading edge transition data can be made. The *AoAs* tested during the painted leading edge campaign were more negative than the polished-leading-edge test points. It was discovered that a combination of both a painted leading edge and a negative *AoA* below -3.5 degrees was required to generate strong crossflow growth on this model. This argument is based on an operating Re_c of 7.5 million. Deployments to colder temperatures and operation at Re_c = 8 million might reduce the need to go to extreme negative *AoA* conditions.

Figure 12 shows a plot of transition Reynolds number, Re_{trans}, as a function of *AoA* for both the polished and painted leading edge. The polished leading-edge transition data show a flat line for Re_{trans} on the right hand side of the figure. At *AoA* values greater than -2 degrees, laminar flow is never extended beyond 80% *x/c*. This results in a maximum Re_{trans} of 6.0 million. As the *AoA* decreases, the Re_{trans} also decreases linearly for the polished leading edge. For the painted leading edge, a similar trend is observed at *AoA* values above -3.5 degrees. Under these conditions it appears as though leading edge surface roughness has little effect, and the dominating instability is a combination of crossflow and T-S waves. However, below an *AoA* of -3.5 degrees, leading edge roughness has a significant role in transition and the dominating instability is crossflow. Below -3.5 degrees *AoA*, there is a significant drop in Re_{trans} for the painted leading edge data that are not observed with the polished leading edge. Figure 12 agrees with past findings that boundary layers with strong crossflow vortices are highly sensitive to leading edge roughness[20].

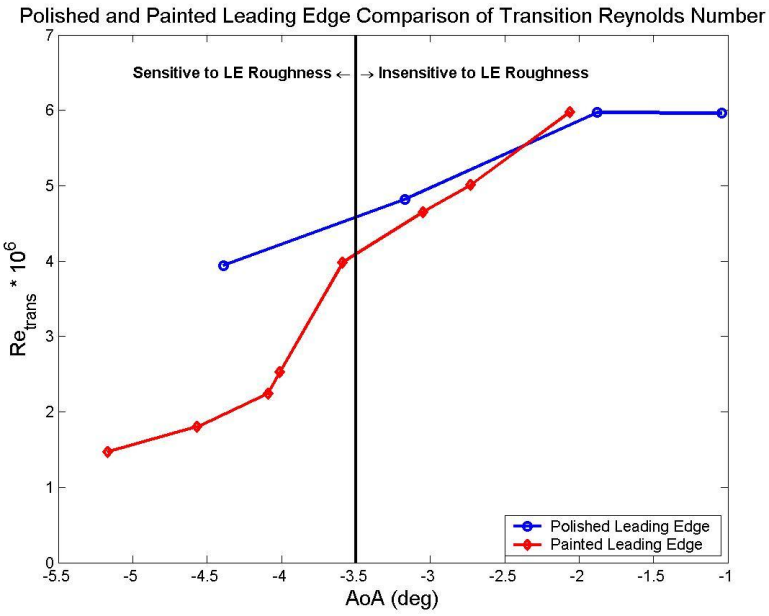

Figure 12: Plot of Transition Reynolds Number for Various *AoAs* and Leading Edge Roughness

V. Critical DREs

The test condition at -2.61 degrees *AoA* was chosen as a good test point for demonstrating the effectiveness of the critically spaced DREs. The goal here was to excite the most unstable crossflow wavelength and move transition forward to match the results obtained in Ref. 6. At this moderately negative *AoA*, transition was observed at 80% *x/c* for both the painted and polished leading edge. For these experiments, the polished leading edge was used with the DRE insert and zero differential pressure applied. There are two methods of applying critical DREs, appliqués and pneumatically actuated. First the appliqué technique is used, and then the pneumatically actuated DREs are described in the next section. Figure 13 shows the transition location for this condition. The flight number depicted in Fig. 13 had appliqué DREs applied to the leading edge, but no effect on the transition location was observed with the IR camera. The baseline flight for this condition showed the same transition location, but the baseline flight produced poor IR images due to less than ideal atmospheric conditions. Thus, the IR image depicted in Fig. 13 is used here as a representative baseline image, despite having DREs applied at the leading edge. Figure 13 shows transition at 80% *x/c* for the area of interest in between the pressure port rows. The goal was then to take this condition and promote the growth of the crossflow instability by introducing periodic roughness spaced at λ_{crit}. The IR camera was used to determine the change in transition location as a function of DRE height, *k*.

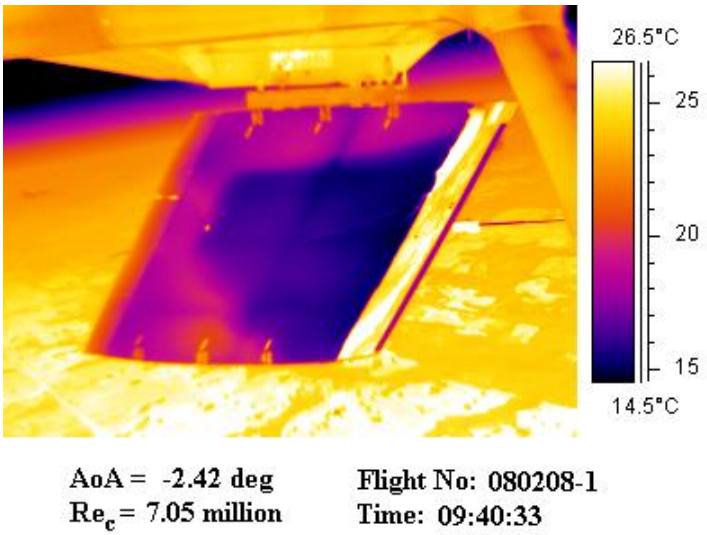

Figure 13: Baseline IR image used to demonstrate critically spaced DREs

The surface roughness of the leading edge was measured as before, except in this case the roughness was measured over the DRE insert, where the DREs were applied, and over the polished aluminum downstream of the DRE insert. The surface roughness over the DRE insert was measured to be 1.24 μm rms with average peak-to-peak values of 4.57 μm. The polished aluminum downstream of the DRE insert was measured to be 0.24 μm rms with average peak-to-peak values of 1.00 μm.

LST theory calculations showed that one of the most unstable crossflow vortex spacing was λ_{crit} = 4.5 mm, measured parallel to the leading edge. Roughness elements were placed 4.5 mm apart at the calculated neutral point of 2.21% *x/c* at the root pressure port row and 2.41% *x/c* at the tip pressure port row. The LST calculations showed that the spanwise variation in the *Cp* distribution resulted in a spanwise variation in the neutral point. Under these flight conditions, the root pressure port row always had a neutral point closer to the attachment line. As a result, the DREs were placed along a line that was not at a constant *x/c*, but rather shifted downstream at the tip to account for the spanwise variation. Figure 14 shows the configuration used for all flights incorporating DREs at the leading edge. In Fig. 14, the DREs are shown along the entire span of the model in order to reduce end effects.

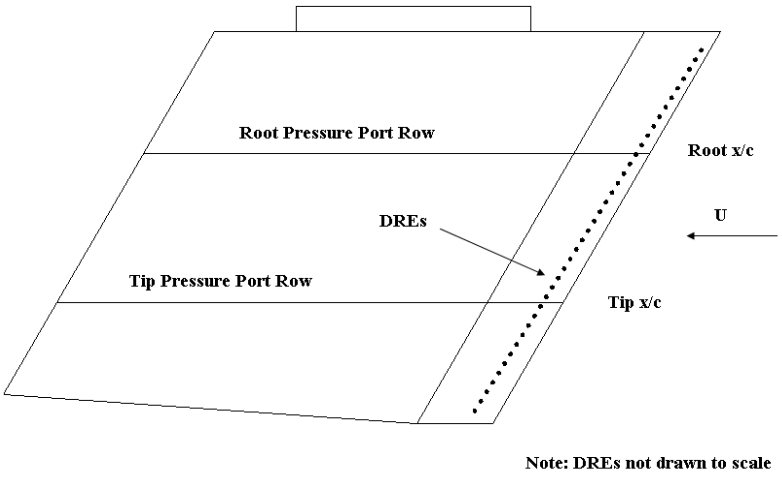

Figure 14: Depiction of DREs applied to the leading edge with a different *x/c* location at the root and tip pressure port rows

The roughness elements used in these experiments were dots commonly used in the graphic arts industry, and will be referred here as appliqué DREs. These appliqué DREs are approximately 6 μm high and can be ordered with any diameter and spacing required. The cross-sectional shape of the appliqué DREs are idealized as right-circular cylinders. The heights of the roughness elements can be increased at 6 μm (as measured by a confocal lens system) increments by stacking individual elements. For the following test conditions k will be specified in all figures. However, it is also instructive to present roughness data with a Reynolds number based on roughness height, Re_k. Re_k is calculated using the absolute velocity at the top of the roughness height, u_k, the kinematic viscosity also at the roughness height, ν_k, and the characteristic length k. Equation 3 shows the relationship for Re_k.

$$Re_k = \frac{u_k k}{\nu_k} \tag{3}$$

Furthermore, the roughness height can be represented as a fraction of the boundary layer height, k/δ. The boundary layer height, δ, is approximately 0.25 mm in the location of the DREs. k, Re_k, and k/δ are supplied for all figures incorporating DREs as a reference for the physical heights of the DREs.

The 2.21% *x/c* location for the root pressure port proved to be ineffective at moving transition with appliqué DREs up to k = 30 μm. Therefore, a full-span array of appliqué DREs spaced at λ_{crit} was applied to the leading edge, but with the root *x/c* location shifted to 2.07%. The tip DREs remained at the 2.41% *x/c* location. The roughness elements used for these experiments had a height of k = 6 μm and a diameter of d = 1.1 mm. For the k = 6 μm case, there was no change in transition and laminar flow was observed back to 80% *x/c*, as in Fig. 13. An additional layer of roughness elements was applied up to k = 12 μm, again with the result that no change in transition was observed. This procedure was repeated until k = 24 μm. At 24 μm, the section of the model below the tip pressure port row became fully turbulent at all *AoAs* tested and all Re_c observable with the IR camera. The top region eventually became turbulent, but only at an unstable negative *AoA*. Furthermore, the turbulent region on the upper half of the model appeared to not have moved forward of the 15% *x/c* location, as the bottom half had done with the appliqué DREs. The turbulent region in Fig. 15 appears to be very close to the attachment line. The reader is reminded that the leading edge was polished aluminum and very little detail can be recovered forward of 15% *x/c* with the IR camera. Therefore, it is unknown where the actual transition location was and only an estimate of less than 15% *x/c* can be made.

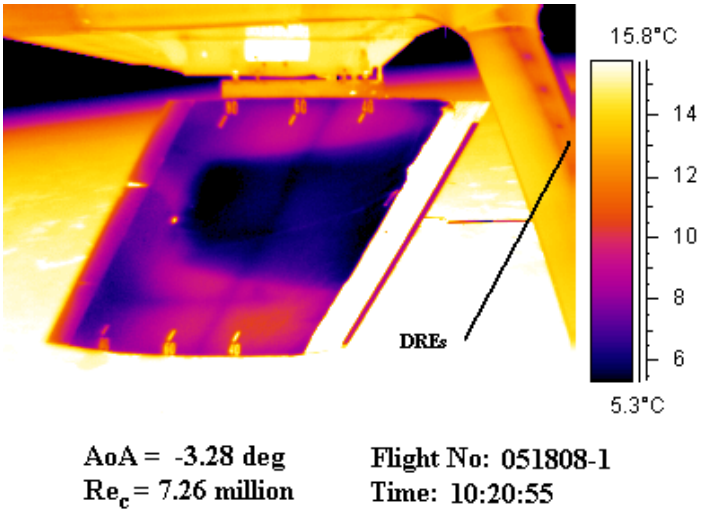

Figure 15: IR image with 24 μm (Root Re_k = 8.8, Tip Re_k = 10.1, k/δ_{root} = 0.08, k/δ_{tip} = 0.08) critical DREs

The DRE heights were then increased to 30 μm by applying another layer of appliqué DREs. Under these conditions the full span of the model was turbulent for all Re_c values recorded with the IR camera. This condition is shown in Fig. 16, again with the result that transition is somewhere forward of 15% *x/c*.

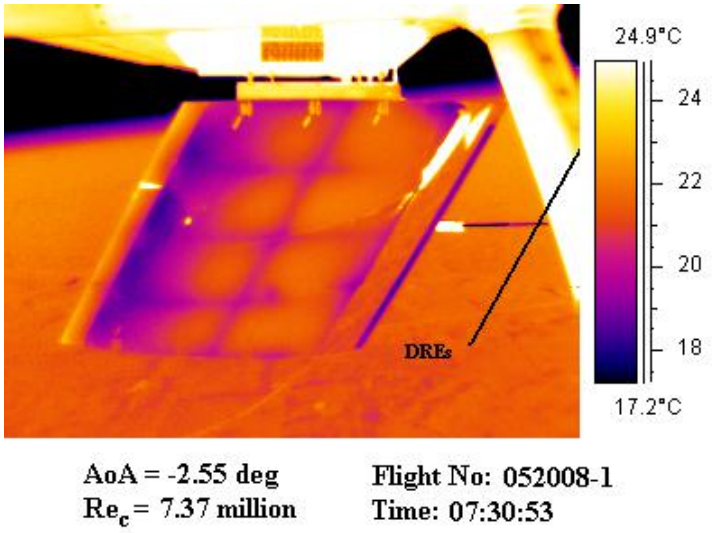

Figure 16: Fully turbulent model with 30 μm (Root Re_k = 14.1, Tip Re_k = 16.3, k/δ_{root} = 0.10, k/δ_{tip} = 0.10) critical DREs

For Figs. 15 through 16, it is worth mentioning that each of these IR images were constant throughout the dive. In each case, transition was observable at approximately 7 million Re_c with the IR camera, and the image looked identical to the ones displayed here. Therefore, the DREs spaced at 4.5 mm appear to be effective at destabilizing the crossflow instability over a wide range of Re_c. Additionally, during these flights the pilot was instructed to change *AoA* on the model. During these *AoA* excursions the transition pattern did not change, also indicating that the 4.5 mm stationary crossflow vortices were destabilizing over a large range of test conditions.

A. Design of Variable Height Roughness Elements

There were two reasons to proceed with implementing a technique of variable roughness height. The first had to do with the receptivity studies. The objective of the receptivity work was to determine coupling between surface roughness height and crossflow disturbance amplitude. This was necessary to provide the proper initial amplitudes to the Nonlinear Parabolized Stability Equations (NPSE) computations. Thus, receptivity was the missing link to the NPSE being used as an independent tool for calculating crossflow stability behavior.

The second reason for variable roughness height arose when the appliqué DREs indicated that there was some critical height leading to the magnification of λ_{crit}. A gradual change in transition was never observed here, contrary to the results obtained in Ref. 6. Transition was either observed at 80% *x/c* or forward of 15% *x/c*. As a result, a design was initiated for changing the roughness heights in a continuous manner, and not only at discrete 6 μm increments. Furthermore, it was desired to have a control system that could change the heights of the DREs while in flight. This required a design change of the leading edge. The design used here was first demonstrated in Ref. 21 and proved to be effective at controlling transition in a low-turbulence wind tunnel. The idea was to create a pressurized chamber where a flexible membrane would seal off holes at the top of the surface. As pressure is applied to the chamber, the flexible membrane would stretch and generate a roughness element. The height of the element would be proportional to the applied pressure and could be controlled in flight. Additionally, vacuum could be applied for generating variable height dimples. This type of roughness element will be referred to as variable height DREs.

Leading edge #2 was modified to accept an insert that nearly covered the entire span of the leading edge. A slot was milled out of the leading edge to hold various DRE inserts. The slot was 2.7% *x/c* thick with the leading edge of the insert at 0.6% *x/c* and the trailing edge at 3.3% *x/c*. The insert was composed of two parts. The top surface

matched the shape of the leading edge curvature. The underside of the top surface incorporated a pressure chamber that was filled with positive or negative gauge pressure. The outer surface of the top piece was drilled with small-diameter holes to create the circular cross-sectional shape of the roughness element. A layer of 48 μm thick Polyester tape was applied over the surface to seal off the top surface and act as the flexible membrane for the variable height DREs. The second part was a flat plate with an O-ring to seal off the bottom of the pressurized chamber. The insert assembly was intentionally designed to sit below the surface of the airfoil in order to account for the tape thickness. A pipe fitting at the trailing edge of the insert provided supply pressure for positive height DREs, or vacuum for creating dimples. A pressure port was added to the leading edge for a static pressure reference. Figure 17 is a schematic of the modified leading edge with the DRE insert.

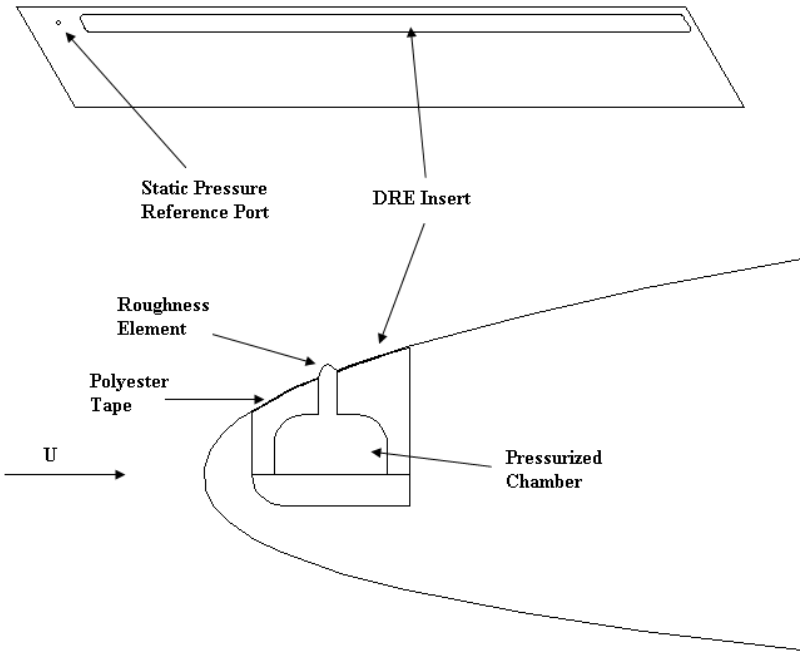

Figure 17: Schematic of DRE insert assembly for variable height DREs

An electronic pressure regulator, capable of both pressure and vacuum control, was installed to drive this pneumatic system. The LJ Engineering 487-002 self-relieving electronic regulator met these specifications. This regulator can supply either pressure or vacuum up to 15 psig. The electronic regulator was controlled by a 0 to 5 VDC signal from the flight computer. To supply pressure to the regulator, a one-gallon air tank was assembled next to the regulator. Before each flight, the air tank was filled to 90 psig. Because no significant mass flow was used in the system, the one-gallon tank could supply pressure to the DRE insert for several hours before requiring a refill. On the other hand, when applying vacuum, the tank could only supply enough vacuum for a few minutes of operation. As a result, the control system was modified to incorporate a vacuum pump with an automatic switch and check valve for maintaining the required vacuum in the supply tank. Typically a flight was either dedicated as a pressure flight or a vacuum flight. However, the entire assembly could be switched in flight from pressure to vacuum in less than five minutes by turning a four-way valve. Calibration of the DRE heights as a function of supplied pressure was performed on the ground with a confocal laser. The calibrations were valid in flight because all supplied pressures were referenced to the pressure at the static port depicted in Fig. 17. Thus changes in atmospheric pressure experienced in flight had no effect on the calibration curve created on the ground.

B. Transition Results with Variable Height Critical DREs

Based on the results obtained with the appliqué DREs, one of the DRE inserts was drilled to match the conditions already tested with the appliqué DREs. The insert was drilled with 1.1 mm holes, spaced 4.5 mm apart, and at the 2.07% *x/c* root and 2.41% *x/c* tip location. It was expected that early transition would be observed

somewhere between 24 and 30 μm, as was observed with the appliqué DREs. With the variable height DREs, the height could be held in between this range to see if transition could be manipulated in a more controlled manner. Figure 18 shows an IR image with the DREs at 31 μm. No change in transition was observed after pressurizing the DREs. The pressure was then increased beyond what was calibrated to an extrapolated DRE height of 75 μm. This condition is shown in Fig. 19. Even under these extreme roughness heights, no change in transition was observed. While the DREs remained pressurized, the pilot was instructed to decrease the *AoA*. Transition moved forward, but only due to the destabilizing nature of the natural crossflow at decreased *AoA* values. The transition front never moved forward of the 15% *x/c* location, which had been done before with the appliqué DREs. The same was true after trying more stable conditions at increased *AoA*s, were transition remained at 80% *x/c* for this case. These results were contrary to the results obtained earlier with the appliqué DREs. The holes were the same diameter, in the same location, and heights were pushed beyond what was tested with the appliqué DREs, yet, no change in transition was observed. Vacuum was also applied down to -60 μm, but still no change in transition was recorded.

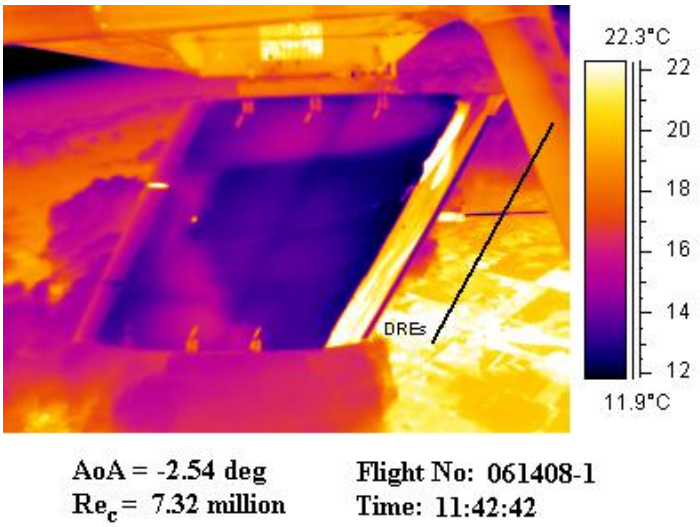

Figure 18: IR image with 31 μm (Root Re_k = 15.1, Tip Re_k = 17.4, k/δ_{root} = 0.10, k/δ_{tip} = 0.10) critical, variable height DREs

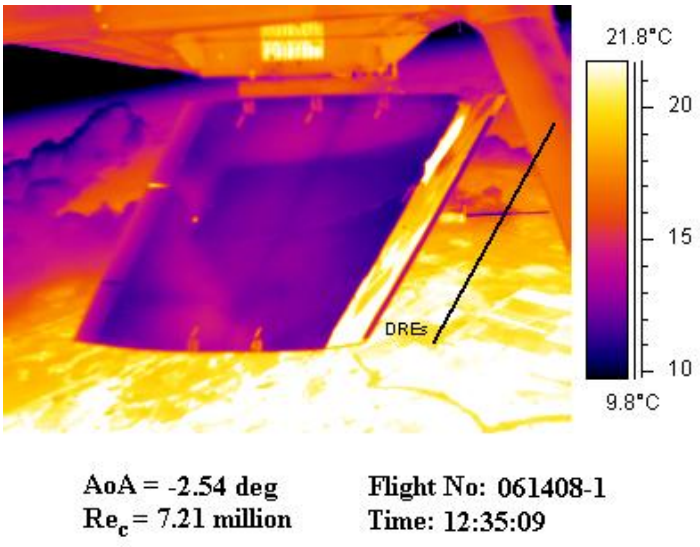

Figure 19: IR image with 75 μm (Root Re_k = 93.4, Tip Re_k = 109.8, k/δ_{root} = 0.24, k/δ_{tip} = 0.24) critical, variable height DREs

After reviewing the lack of transition manipulation, a suggestion was made to increase the hole diameter. When one looks at the cross-section of the variable height DREs, there is a definite difference between the variable height DREs and the appliqué DREs. Figure 20 shows DRE scans with the Mitutoyo surface roughness tester of the two different DRE types tested. The appliqué DREs are idealized as a right-circular cylinder whereas the variable height DREs are shaped more like a Gaussian curve. It is possible that the effective diameter of the variable height DREs was less than the appliqué DREs, explaining the lack of transition modification with these roughness elements. As a result, a 12 inch section of the DRE insert was drilled to 2 mm holes to test larger diameters. However, as seen before, no change in transition occurred at all *AoA*s tested and further investigation was needed to understand the importance of roughness shape.

Flights with the critical DREs demonstrated a high sensitivity to both the shape and height of the roughness elements. At an *AoA* of -2.61 degrees, the model was laminar back to 80% *x/c* with roughness elements below a critical height. Above the critical height, the model was turbulent forward of the 15% *x/c* location. With d/λ ratios of 0.24, the critical height was found to be k = 30 μm. With a d/λ ratio of 0.44, the critical height was lower at k = 18 μm. These results agree with the findings of Radeztsky et al.[22] where d/λ ratios approaching 0.5 were most effective at introducing strong crossflow growth. On the other hand, the variable height DREs demonstrated no change in transition up to 100 μm with pressure applied, and -60 μm with vacuum applied, even with the larger 2 mm diameter DREs. The sensitivity to roughness height was already known prior to these experiments[22], however, the sensitivity to roughness shape was not known, and more experiments were needed to better understand the receptivity process affecting transition.

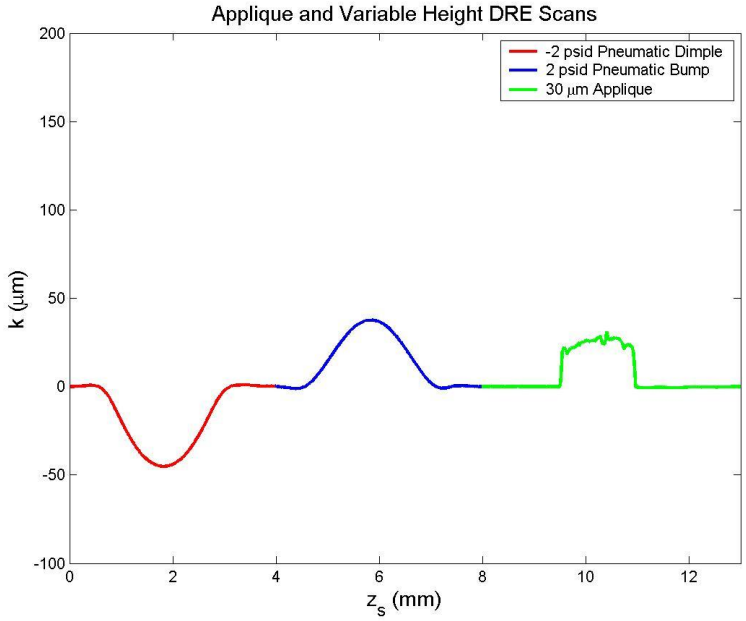

Figure 20: Surface scans of 2 mm diameter, variable height DREs and an appliqué DRE with a diameter of 1.1 mm

VI. Receptivity Measurements

The multi-element hotfilm array has proven to be a valuable tool for transition location, shock detection, and crossflow vortex spacing identification. Transition can be identified with a hotfilm by looking at the spectral content of the voltages acquired from either a constant temperature, constant current, or constant voltage anemometer. The same procedure can be used for identifying shocks[23]. Both amplitude and phase information can be used for identifying crossflow vortex spacing on a swept-wing. However, in each of these experiments the actual shear stress value is not calculated, only raw voltages are recorded. It was desired here to measure the mean shear stress and disturbance shear stress generated by DREs placed at the neutral point upstream of a hotfilm array, in order to

resolve the importance of roughness shape and height. Uncalibrated hotfilms could not achieve these results due to variations in sensor resistances between each channel. It is possible that an uncalibrated hotfilm could measure the crossflow vortex spacing as was done in Refs. 24 and 25, but to measure the disturbance amplitude required a calibrated hotfilm array. Therefore, a calibration scheme was needed for calibrating the hotfilms in flight and making measurements of the disturbance amplitude generated by modulating DRE heights. A Preston tube would be used to provide the known shear stress for calibration.

A. Hotfilm Array Design

A custom hotfilm was designed for measuring the crossflow amplitude and spacing on the SWIFT model. With a maximum crossflow spacing of 4.5 mm, a multi-element hotfilm array was needed for measuring the high and low shear stress regions in between areas of strong crossflow growth. The spacing of each hotfilm sensor needed to be small enough to resolve the shape of the crossflow wavelength, in addition to having a long enough span to capture at least one period. The 4.5 mm crossflow spacing is measured parallel to the leading edge. When each hotfilm sensor is placed perpendicular to the inviscid streamline, the crossflow spacing at the hotfilm is approximately 3.9 mm, resulting in an even finer spacing required for the hotfilm design.

The Cessna O-2A aircraft could only carry an additional 100 lbs of instrumentation, at the expense of performing one dive per flight. Flights prior to these receptivity measurements always had enough fuel to perform two dives per flight. The FRL has 30 channels of CTAs divided between three chassis. Each chassis weighs 50 lbs so only two chassis could be installed in the aircraft. Therefore, the goals set for measuring the crossflow vortices needed to be met with a maximum of 20 channels.

The multi-element hotfilm used in these experiments was constructed by Tao Systems. The design utilized the smallest sensors and lead widths that the manufacturer had confidence in constructing. Sensors with a 0.002” (50 μm) diameter and a length of 0.02” (0.51 mm) were used with the smallest lead widths available. Figure 21 shows the details of the hotfilm sensor designed for these experiments. The smallest dimensions available for the design resulted in a staggered hotfilm where the line intersecting the center of each sensor was swept back 42 degrees. If this line where swept back at 30 degrees, then the sweep of each sensor would have matched the Λ_{LE}, and each sensor would be located at the same *x/c* location on the model. However, the limitations in manufacturing tolerances forced the sensors to be along a 42-degree swept line resulting in a change in *x/c* location of 0.2% for 20 channels. The change in disturbance growth over 0.2% *x/c* is calculated to be negligible, therefore the change in *x/c* location for the hotfilm is assumed to be zero.

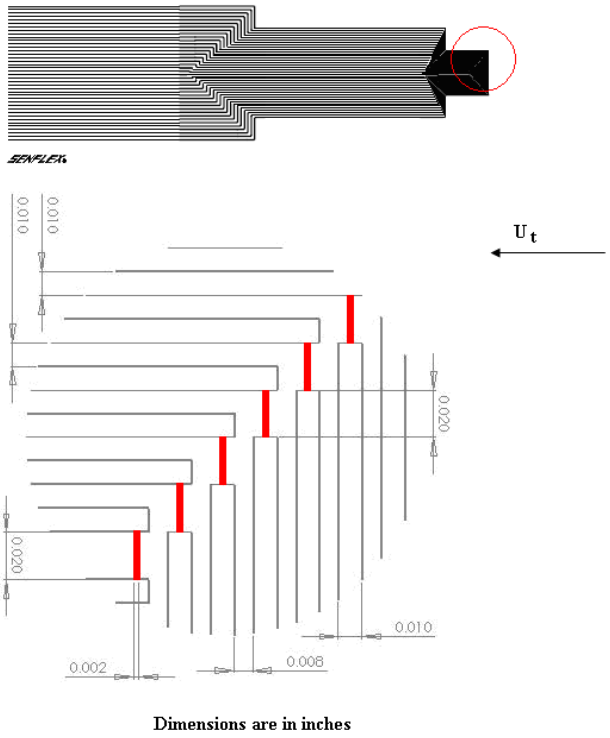

Figure 21: Custom hotfilm design for measuring disturbance amplitudes and crossflow vortex spacing

It was desired to use the 2 mm diameter, variable height, DREs centered on the root pressure port row for the hotfilm calibration and receptivity measurements. The larger diameter, variable height DREs would be more effective at introducing a disturbance than the smaller 1.1 mm diameter variable height DREs located lower on the DRE insert. Therefore, the hotfilm would be mounted somewhere along the root pressure port row. Despite showing zero change in transition location with the variable height DREs, an active control system was needed to turn off the DREs for hotfilm calibration. A uniform shear stress was needed across the hotfilm to calibrate each sensor. This was accomplished by calibrating the hotfilm at a stable *AoA* demonstrating little crossflow growth, e.g. -2.61 degrees *AoA*, with the critically spaced DREs turned off. This idea was adopted from the calibration suggestions made by Chapman[26]. There is no way of "turning off" the appliqué DREs, therefore the variable height DREs were needed for the hotfilm calibration. Furthermore, a comparison between the disturbance amplitude with the appliqué DREs and variable height DREs could be made.

Provided the boundary layer is still laminar, the Branch II point, or location of highest disturbance growth, is the preferred location for the hotfilm. However, since the 2 mm diameter DREs were only drilled along a 12 inch span centered on the root pressure port row, there was a limit on how far aft the hotfilm could be mounted. Figure 22 shows the hotfilm located at 34% *x/c*, which proved to be the farthest aft mounting location for the hotfilm based on a 12-degree half-angle wedge generated by the first and last DRE, as suggested by Saric[27]. Furthermore, the model is still laminar at 34% *x/c* at the two *AoA*s of interest, which is a necessary requirement for measuring the crossflow vortices.

The spacing between the surface mounted thermocouple, static pressure port, Preston tube, and first hotfilm channel were all 0.9 inches along a line of constant *x/c*. Prior to mounting the hotfilm, which is a pseudo-permanent attachment, a wind tunnel test was conducted to see how close each of these components could be displaced from each other. At the tunnel's maximum speed of 40 m/s, it was found that the Preston tube could be displaced 0.5 inches from the static pressure port. Similarly, the Preston tube had to be 0.8 inches from the first hotfilm channel before the shear stress measurement was affected by the presence of the Preston tube. The 0.9 inches was selected as the appropriate distance in order to fair in the edges of the hotfilm and surface mounted thermocouple with Bondo to avoid any forward facing steps. Any closer, and it would have been difficult to sand down the faired in edges of the

hotfilm and surface-mounted thermocouple. The spacing between each component is assumed to be small enough that each component experiences the same shear stress, provided the crossflow growth is minimal during the calibration.

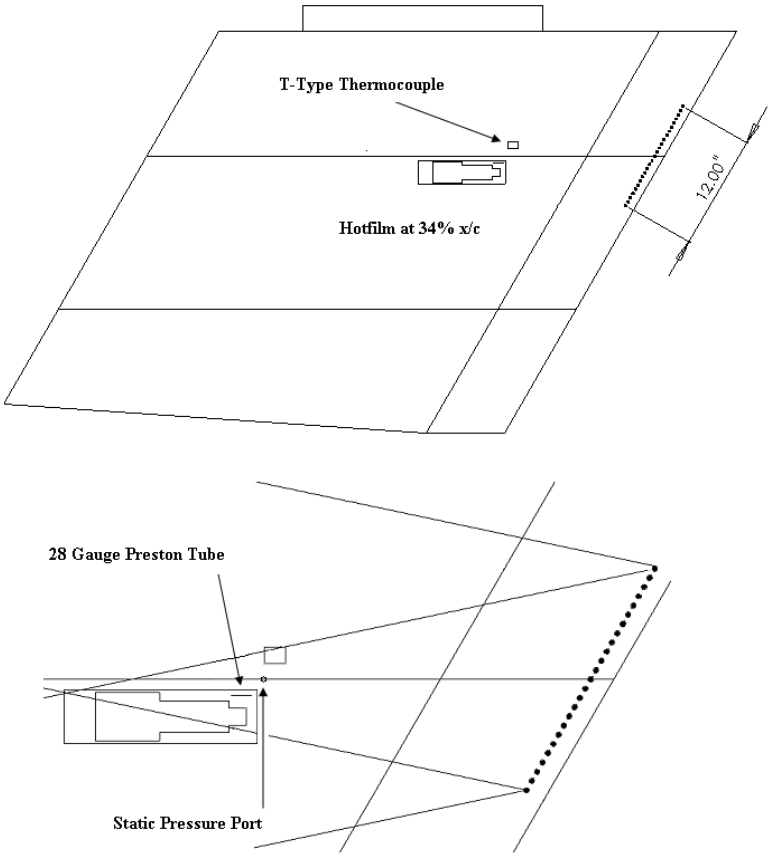

Figure 22: Schematic of hotfilm, Preston tube, surface-mounted thermocouple, and static pressure port on the SWIFT model

B. Preston Tube

The flight experiments here are subject to large temperature excursions during the dive profile. As a result, a comparison of the raw voltages from each sensor would be meaningless. A Preston tube was placed next to the hotfilm to provide the known measure of shear stress for the calibration scheme. Preston first developed the procedure for using a surface-mounted Pitot-tube for measuring shear stress at the surface of external and internal flows[28]. Patel re-addressed the calibration from Preston's original paper and has developed the most widely used set of equations for measuring shear stress with a Preston tube. Patel also addressed the issue of operating a Preston tube in pressure gradients, where the accuracy of the Preston tube decreases in favorable pressure gradients as compared to adverse pressure gradients[29].

Most of the literature deals with Preston tubes mounted in either external or internal turbulent boundary layers. However, Bechert provides an asymptotic equation which combines the three pressure ranges covered by Patel, in addition to providing an equation for use of a Preston tube in laminar flow, which is used here[30]. Bechert's equation in laminar flow proved to be the most accurate based on a comparison between experimental measurements of wall

shear stress, τ_w, and computations. Equations 4 and 5 were used for calculating τ_w in the laminar boundary layer on the SWIFT model.

$$\tau^+ = 4\sqrt{\frac{\Delta p^+}{3}} \tag{4}$$

$$\tau^+ = \frac{\tau_w d_{Prest}{}^2}{\rho\nu^2}, \Delta p^+ = \frac{\Delta p d_{Prest}{}^2}{\rho\nu^2} \tag{5}$$

In Equation 5, Δp is the differential pressure measured between the Preston tube and the nearby static pressure port. d_{Prest} is the outer diameter of the Preston tube. ρ and ν are the fluid density and kinematic viscosity of the freestream, respectively. Bechert specifies limits for Δp^+ in which Equation 4 is valid. The Δp^+ values recorded in these experiments range from $5*10^4$ to $3*10^5$, which is slightly outside the range specified by Bechart[30].

The requirements for using a Preston tube are that the tube must sit within the viscous sub-layer of the boundary layer, with a general rule of thumb that the diameter of the Preston tube must be a small percentage of the boundary layer height. This requirement becomes even more difficult to meet with a laminar boundary layer, requiring an even smaller Preston tube. The Preston tube used here was a 28-gauge hypodermic stainless steel needle with a flat, round mouth. The outer diameter was 0.014 inches which was 36% of the boundary layer height at the 34% *x/c* location. Smaller hypodermic needles were available, but the time response became too high to be useable in the dive attitude where conditions were constantly changing. As a result, a compromise was made to find a Preston tube small enough to meet the requirements set by Patel on the percentage of boundary layer height, but to be large enough to have a sufficient response time to provide time-accurate data in the dive. The 28-gauge hypodermic needle proved to be a good compromise because the time lag in this tube proved to be small enough to be useful in the dive, and the diameter was not excessively large compared to δ.

Two Honeywell Sensotech FP2000 pressure transducers were mounted inside the internal cavity of the SWIFT model to reduce the tube length to the transducers. Furthermore, the 28-gauge Preston tube was only one inch long. The Preston tube was quickly stepped up to a two inch long, 0.040 inch outer diameter, stainless steel tube. This was followed by six inches of 0.040 inch inner diameter polyurethane tubing. Lastly, a five foot section of 0.063 inch inner diameter polyurethane tubing led to the pressure transducers inside the model. Furthermore, the tubing for the static pressure port was purposely extended to match the time lag of the smaller-diameter Preston tube.

In addition to the large diameter of the Preston tube used here, there is a question regarding the accuracy of the Preston tube in the favorable pressure gradient tested here, based on the recommendations in Ref 29. However, the goal of the current experiments is to find a difference in shear stress between the peaks and valleys generated by the crossflow vortices. Therefore, any error in the absolute calibration of the hotfilm will be subtracted out when taking the difference. With this overall goal in mind, the decrease in accuracy with the relatively large Preston tube and use in a favorable pressure gradient has been accepted.

C. Temperature Compensation

Prior to flight, several measurements were made of the voltage output of each hotfilm channel in the FRL's un-insulated hangar, subject to temperature changes as much as 2°C/hour. Each channel on the hotfilm array was adjusted with a gain of 10 and an overheat ratio of 1.2 to provide sufficient sensitivity during flight. With this gain, the zero flow voltage, E_o, of each channel would change by approximately -0.45 V/°C, as depicted in Fig. 23. Note that in all of the following figures displaying voltages from the CTAs, an offset of 5 Volts has been added to each channel. The analog input channels on the DAQboards used in these experiments are all bipolar. In order to get the highest resolution out of these 12-bit DAQboards, the DC offset of each channel has been set to an average of 0 Volts. To avoid sign changes after acquisition, an offset of 5 Volts has been added to each channel.

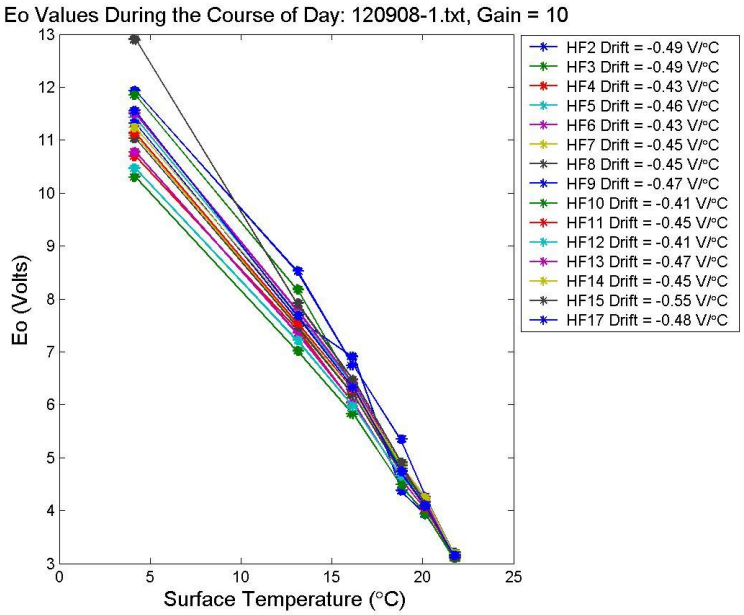

Figure 23: Eo measurements recorded in the FRL hangar

The temperature drift displayed in Fig. 23 agrees with the measurements made in Radeztsky et al.[31] where a linear temperature drift was observed with CTAs and hotwires. Based on the findings in the hangar prior to flight, temperature compensation would be the most important problem to address in order to resolve any useful data. Moreover, the temperature drifts reported in Ref. 31 were recorded at constant velocity as the un-cooled tunnel heated up. This was not possible here because the aircraft would run out of fuel before a large temperature difference, at constant attitude, could be achieved in flight. As a result, the temperature drift would have to be conducted on the ground with zero air flow over each channel. To prevent sensor burnout, each hotfilm channel was disconnected from the CTA circuit in between each recording, which were typically spaced one hour apart.

The Preston tube data were recorded during three phases of each flight. During the cold soak, while the crew was waiting for the model to cool down uniformly, the pilot would increase the airspeed at five knot increments at a constant *AoA*. Once the model was at a uniform cold temperature, the dive was initiated, again at a constant *AoA*. The FTE recorded data continuously during the dive at 20 Hz. At the end of the dive the pilot would decelerate, also at constant *AoA*, while the FTE continued to record the slow down period. During the return to base, the pilot would perform another calibration run, but this time the temperature was higher at the lower altitude. Figure 24 shows the Preston tube τ_w plotted against the true airspeed in knots, *KTAS*, recorded with the five-hole probe. In Fig. 24, data outside the targeted β range of 2.61 ± 0.10 degrees have not been included in the plot. Additionally, Fig. 25 shows the calibration curve that was needed to correlate τ_w measured from the Preston tube and each of the 17 hotfilm voltages, *E*, recorded during the dive.

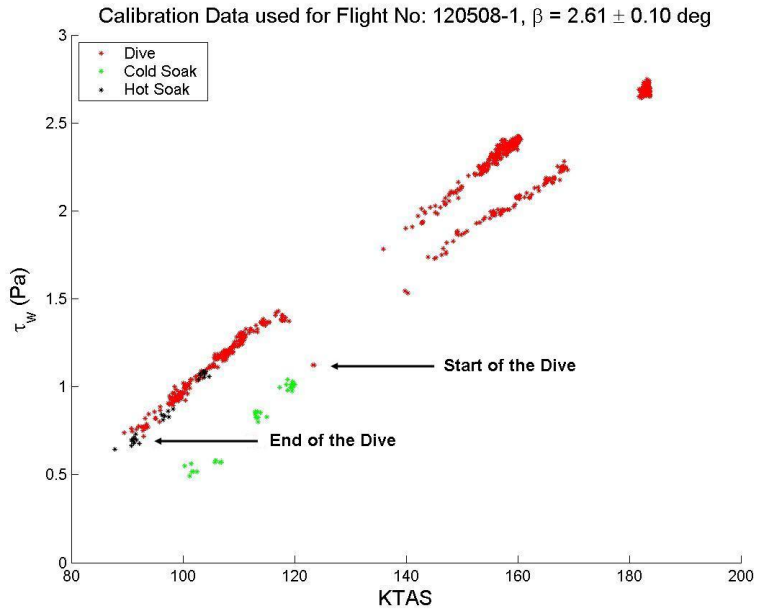

Figure 24: Filtered Preston tube data during the cold soak, dive, and hot soak

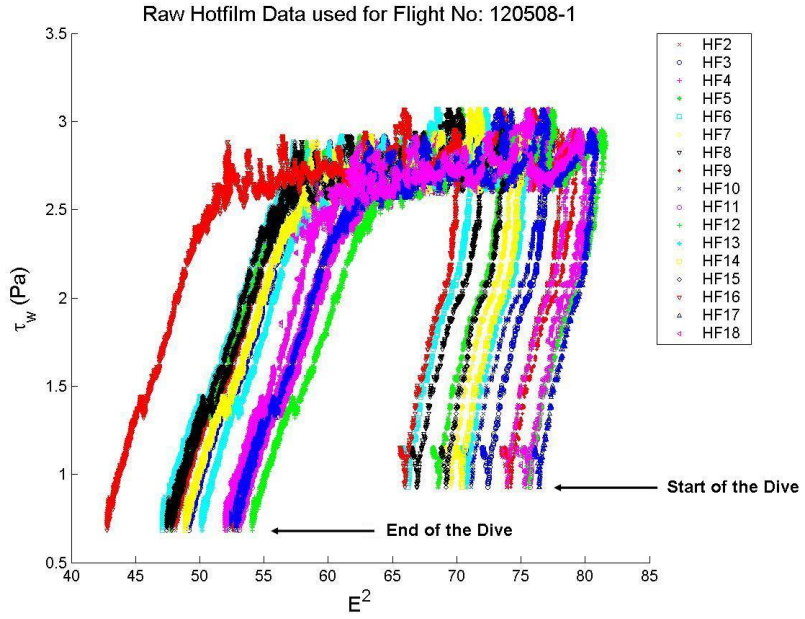

Figure 25: Wall shear stress and recorded hotfilm voltages during the dive

In both Figs. 24 and 25, there are obvious hysteresis loops which need to be corrected before a calibration can be attempted. In Fig. 24, τ_w is higher at the bottom of the dive because the dynamic viscosity is higher at the warmer temperatures at low altitude. In Fig. 25, the hotfilm voltages are lower at the bottom of the dive because less voltage is required at the warmer temperatures to maintain the overheat ratio in each hotfilm channel. In light of Figs. 24 and 25, a temperature compensation scheme was required to generate a calibration curve that was independent of temperature.

Radeztsky et al[31] suggest that the temperature drifts recorded for each hotfilm channel can be used to correct the measured voltages to a compensated voltage based on a standard temperature. Equation 6 has been proposed here to calculate a temperature compensated voltage for each hotfilm channel.

$$E_{comp} = E_{measured} + m(T_{nom} - ST) \tag{6}$$

In Equation 6, $E_{measured}$, is the recorded voltage subject to temperature changes. m is the temperature drift for each hotfilm channel displayed in Fig. 23. T_{nom} is a nominal temperature that all voltages are corrected to. In these experiments, 10°C was used throughout. *ST* is the surface temperature of the model next to the hotfilm. The surface temperature was selected as the more appropriate temperature to use because shadows and solar radiation from direct sunlight affect the measured voltage of each hotfilm channel. Since the surface-mounted thermocouple is mounted next to the hotfilm, the surface-mounted thermocouple will experience the same solar radiation and be more representative of the actual temperature experienced by each hotfilm sensor.

After inserting the temperature drift values recorded in Fig. 23 for each individual channel and re-plotting in the manner of Fig. 25, the calibration curves still did not collapse on top of each other. Then m was adjusted for each channel until the calibration curve for the top and bottom of the dive eventually collapsed on top of each other into one curve, indicating a temperature invariant calibration curve. After doing this for each channel, the temperature drift for 17 hotfilm channels averaged to m = -0.28 V/°C. This is in comparison with the average temperature drift recorded in the hangar of m = -0.45 V/°C. The in situ adjustment of m for each flight was expected because the heat conduction lost to the model is different for each flight. Therefore, it cannot be expected that the temperature drift recorded on the ground, in the hangar, would be universally applicable to all flights. This empirical discovery is in agreement with Ref. 32, where heat conduction to the substrate is the biggest problem in calibrating surface-mounted hotfilms, and must be accounted for on each model for every test. Once each temperature drift value is finalized for each flight, a calibration curve typical to the one depicted in Fig. 26 is generated, that is now temperature invariant.

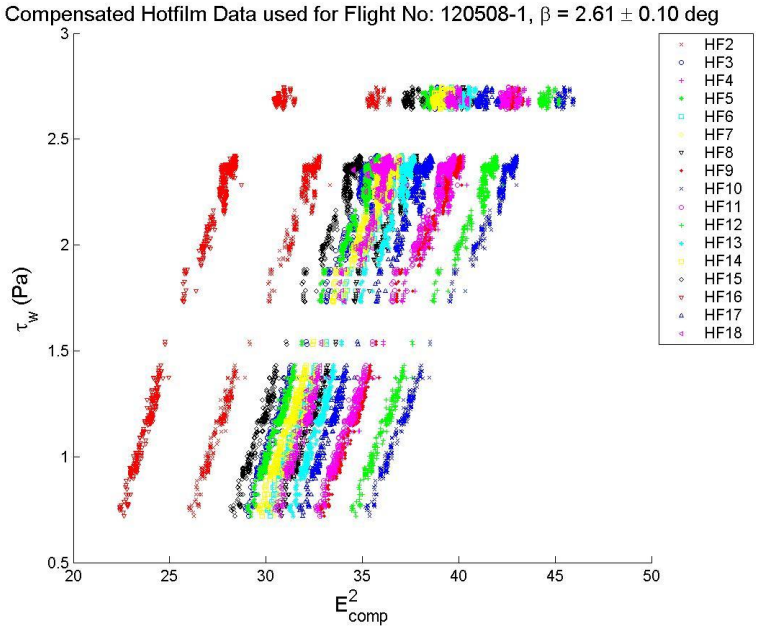

Figure 26: Finalized calibration curve after applying temperature compensation

D. Hotfilm Calibration

Bellhouse et al[33] was the first to address the relationship between the voltage output of a CTA and τ_w. as shown in Eq. 7.

$$E_{comp}{}^2 = A\tau_w{}^{1/n} + E_o{}^2 \tag{7}$$

Now τ_w is solved for as the dependent variable,

$$\tau_w = \left(\frac{E_{comp}{}^2}{A} - \frac{E_o{}^2}{A} \right)^n \tag{8}$$

The constant n is typically ≥ 3. If n is assumed to be 3, then Eq. 8 can be expanded using the Binomial Theorem using $E_{comp}{}^2$ as the independent variable calculated from Eq. 6,

$$\tau_w = a\left(E_{comp}{}^2\right)^3 + b\left(E_{comp}{}^2\right)^2 + c\left(E_{comp}{}^2\right) + d \tag{9}$$

Now a third-order polynomial curve fit can be applied to find the constants a, b, c, and d in Eq 9 for each channel. The constants A and E_o have been absorbed into the constants a, b, c, and d. Fig. 27, shows a least-squares curve fit using a third-order polynomial which fits nicely with the temperature compensated data recorded during the dive. This procedure is then repeated for all the hotfilm channels.

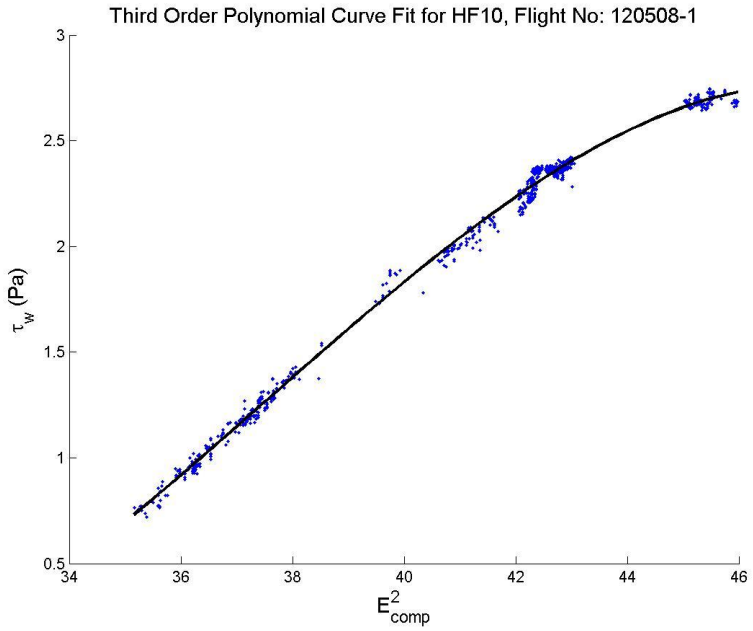

Figure 27: Example calibration curve for one of the hotfilm sensors

In all of the calibration curves generated here, the data used for calibrating each hotfilm sensor were subject to two filters. The DREs had to be turned off, and the *AoA* on the model had to be within a ± 0.1 degree band about the targeted *AoA* for that flight. Using this procedure to eliminate data with strong crossflow growth with the DREs on, and bad data away from the targeted *AoA*, clean calibration curves were generated for all hotfilm channels and all flights tested so far.

E. Receptivity Results

After installing the hotfilm, Preston tube, and surface-mounted thermocouple, a 20-degree lens on the IR camera was installed to get a close image of this area. The intent here was to confirm that the boundary layer over the hotfilm was still laminar after installation and fairing in the edges with Bondo. Figure 28 shows an IR image with the 20-degree lens confirming that the boundary layer in this area remained laminar. Figures 29 and 30 show representative IR images with the 60-degree lens for the two *AoA*s tested here. Figure 29 shows the hotfilm located just upstream of transition at -4.76 deg *AoA*. Figure 30 shows laminar flow back to 80% *x/c* at an *AoA* of -2.59 degrees. At this *AoA* the hotfilm is located in a stable region with little crossflow growth. In both Figs. 29 and 30 the variable height DREs were pressurized up to 50 μm, but as before, no change in transition was observed with the IR camera. The transition results with the IR camera were also confirmed with Power Spectral Density plots of one of the hotfilm channels, also confirming a laminar boundary layer.

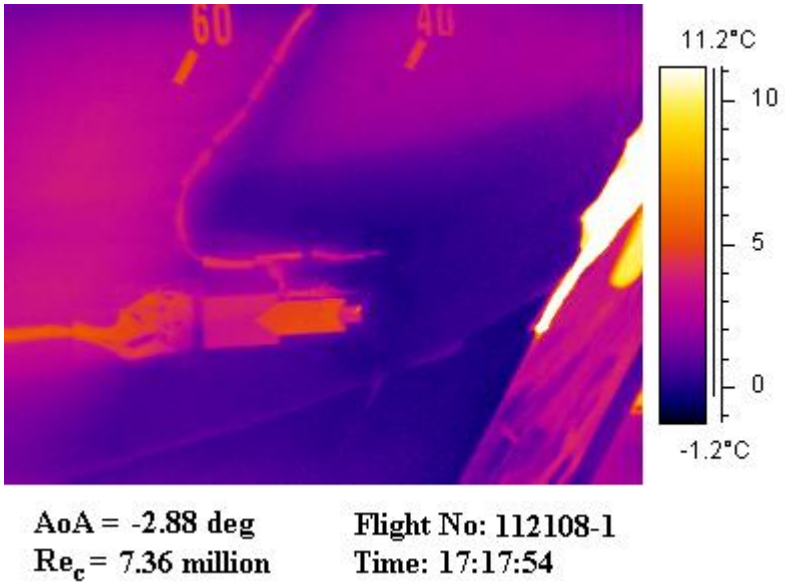

Figure 28: IR image showing a laminar boundary layer over the hotfilm, Preston tube, static pressure port, and surface-mounted thermocouple

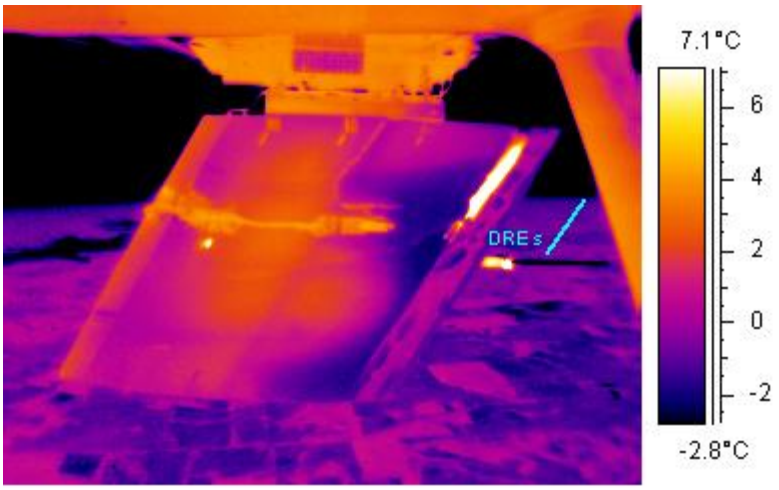

Figure 29: IR image of the hotfilm located just upstream of transition

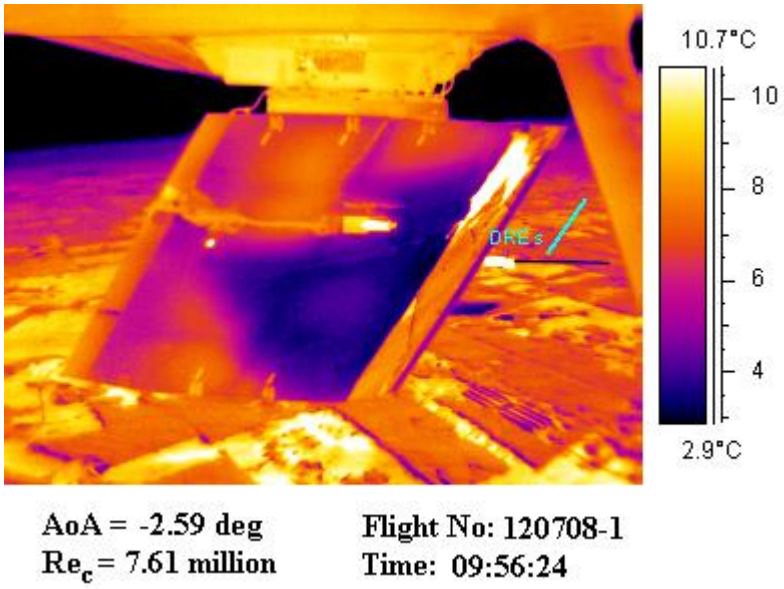

Figure 30: IR image of the hotfilm located in a stable laminar boundary layer

Two *AoA* conditions have been tested thus far. The test point at -2.61 degrees *AoA* proved to have very little crossflow growth at the 34% *x/c* location. Even with the variable height DREs pressurized to 50 μm, no crossflow structure is apparent in the hotfilm signal. Vacuum was also tested with the DREs drawn down to -50 μm, but with similar results with no signs of crossflow. For this *AoA*, the hotfilm is probably mounted too close to the leading edge and the crossflow vortices have not grown enough to be recorded with the hotfilm. On the other hand, the test point at -4.69 degrees *AoA* shows strong signs of crossflow, even without the DREs pressurized or evacuated. A definite structure spaced 4.5 mm is apparent in the signal. Furthermore, the signal gets stronger as the DREs are pressurized. The same is true during the evacuated flights where the DREs were drawn down to -50 μm. A strong 4.5 mm structure was also observed. Figure 31 shows a comparison of the skin-friction coefficient, c_f, versus spanwise position parallel to the leading edge between two flights with pressurized DREs.

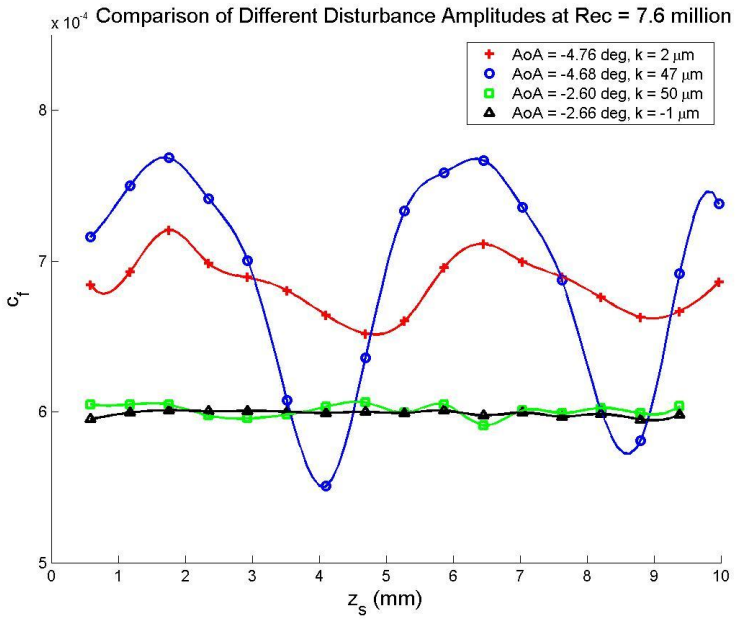

Figure 31: Comparison of different disturbance amplitudes with DREs spaced 4.5 mm apart

Figure 31 shows that the hotfilm covered two crossflow vortices. However, videos created after each flight showed as much as four different crossflow vortices being captured by the hotfilm, but still at the 4.5 mm spacing. As α fluctuates during the dive, four crossflow vortices move in and out of the frame, with only two vortices captured during a given time. This small spanwise modulation of the stationary crossflow vortices explains why the heat generated by the crossflow vortices does not appear in the IR images.

In Figure 31, the first curve at an *AoA* of -4.76 deg is in phase with the second curve with the DREs pressurized. The electronic pressure regulator used in these experiments has difficulty holding zero differential pressure. There is always some residual pressure in the system on the order of 0.05 psid, resulting in DRE heights of less than ± 2 μm. This small roughness height appears to be strong enough to force a spanwise invariant structure, which is not expected for naturally occurring crossflow vortices due to random surface roughness. Naturally occurring crossflow vortices would not be in phase with vortices generated by excited roughness elements. However, all test points at the -4.69 deg *AoA* test condition show a strong 4.5 mm structure that is always in phase with the DREs on and off. Thus, a comparison can now be made between disturbances generated by a 2 μm bump versus a 50 μm bump. It appears as though there is a non-linear relationship between the roughness height and the disturbance amplitude measured downstream of the roughness elements. The signal generated by the 2 μm roughness element is close to the signal generated by the 50 μm bump, despite having a much smaller height. However, the signals measured at -4.69 deg *AoA* are measured just upstream of transition, so the amplitudes may have already saturated. Nevertheless, the technique outlined in this paper for calibrating hotfilms produces good results and more flights can be conducted to further understand the receptivity process due to DREs.

VII. Conclusions

A flight-test platform has been created with a 30-degree swept-wing test article and a Cessna O-2A aircraft for the intent of studying boundary-layer transition. In parallel, a computational model has been created that has generated *Cp* distributions and stability calculations that match the experiments. Appliqué DREs have shown to be effective at modifying transition by a 100% increase in the laminar flow region. The procedure outlined here for temperature compensation and hotfilm calibration has proven to be effective for measuring disturbance amplitudes in flight. Stability calculations can now proceed to compute the disturbance-velocity amplitude from the shear stress measurements. Furthermore, a comparison between the disturbance amplitude with the appliqué DREs and the variable height DREs is left to be completed for future flights.

Acknowledgements

This research endeavor would not be possible if it were not for the exceptional team at the Texas A&M Flight Research Laboratory. The author would like to acknowledge Andrew Carpenter who contributed extensively to this work which was the basis for his PhD dissertation. Professor Helen Reed and her student Richard Rhodes conducted all of the computational work on this project. The Flight Research Laboratory team consisted of graduate students Michael Belisle, Jerrod Hofferth, Lauren Hunt, Tyler Neale, Shane Schouten, Matthew Woodruff; undergraduate students Brian Crawford and Brandon Erwin; mechanic Cecil Rhodes; administrative assistant Colleen Leatherman; and the pilots Roy Martin, Dr. Donald Ward, Celine Kluzek, and Lee Denham. Both Dr. John Schmisseur, AFOSR Program Manager and Gary Dale, AFRL Program Manager added valuable insight and direction to the program..

References

[1]Green, J.E., "Laminar Flow Control – Back to the Future?" *AIAA 2008-3738*, 2008.

[2]Saric, W.S., Carrillo, R.B., Reibert, M.S., "Leading-Edge Roughness as a Transition Control Mechanism," *AIAA 98-0781*, 1998.

[3]Saric, W.S., Reed, H.L., Banks, D.W. "Flight Testing of Laminar Flow Control in High-Speed Boundary Layers," *NATO-RTO-MP-AVT-111/RSM*, 2005.

[4]Reed, H.L., Saric, W.S., "Transition Mechanisms for Transport Aircraft," *AIAA 2008-3743*, 2008.

[5]Saric, W.S., Reed, H.L., White, E.B., "Stability and Transition of Three-Dimensional Boundary Layers," *Ann. Rev. Fluid Mech., 2003.35:413-40*.

[6]Reibert, M.S., Saric, W.S., Carrillo, R.B., Chapman, K.L., "Experiments in Nonlinear Saturation of Stationary Crossflow Vortices in a Swept-Wing Boundary Layer," *AIAA 96-0184*, 1996.

[7]Wassermann P, Kloker M. "Mechanisms and control of crossflow-vortex induced transition in a three-dimensional boundary layer," *J. Fluid Mech.* 456:49-84, 2002.

[8]White, E.B., Saric, W.S. "Secondary Instabilities of Crossflow Vortices," *J. Fluid Mech. Vol. 525*:275-308, 2005

[9]Morkovin, M.V., "On the many faces of transition," *Viscous Drag Reduction*, ed: CS Wells, pages 1-31, New York: Plenum, 1969.

[10]Choudhari, M., Streett, C., "Boundary Layer Receptivity Phenomena in Three-Dimensional and High-Speed Boundary Layers," *AIAA 90-5258*, 1990.

[11]Rhodes, R.G., Carpenter, A.L., Reed, H.L., Saric, W.S., "CFD Analysis of Flight-Test Configuration for LFC on Swept-Wings," *AIAA 2008-7336*, 2008.

[12]Martin, M.L., Carpenter, A.L., Saric, W.S., "Swept-Wing Laminar Flow Control Studies Using Cessna O-2A Test Aircraft," *AIAA 2008-1636*, 2008.

[13]McKnight, CW 2006. Design and Safety Analysis of an In-Flight, Test Airfoil. Master's Thesis, *ETD-TAMU-2006B-AERO-McKnight*.

[14]Saric, WS, Carpenter, A.L, Hunt LE, McKnight CW, Schouten SM 2006b. "SWIFT – Safety Analysis for Swept-Wing Experiments." *TAMUS-AE-TR-06-002*, Technical Report, January 2006.

[15]Saric, W.S., Carpenter, A.L., Reed, H.L., "Laminar Flow Control Flight Tests for Swept Wings: Strategies for LFC," *AIAA 2008-3834*, 2008.

[16]Banks, D.W., van Dam, C.P., Shiu, H.J., Miller, G.M., "Visualization of In-Flight Flow Phenomena Using Infrared Thermography," *NASA/TM-2000-209027*, 2000.

[17]Brandon, J.M., Manuel, G.S., Wright, R.E., Holmes, B.J., "In-flight flow visualization using infrared imaging," *Journal of Aircraft 27:612-618,* 1990.

[18]Miley, S.J., van Dam, C.P., Yip L.P., Willard, P.E., Crowder, J.P., Wazlavick, R.L., "Slat transition characteristics on the NASA B737-100 aircraft using infrared imaging and hotfilm anemometry," *Crowder JP (ed) Flow visualization VII. Begell House, New York, pages 950-956,* 1997.

[19]Schlichting, H., Gersten, K., "Boundary Layer Theory," Springer-Verlag, 2000.

[20]Saric, W.S., Reed, H.L., "Crossflow Instabilities – Theory & Technology," *AIAA-2003-0771*, 2003.

[21]White, E.B., Saric, W.S., "Application of Variable Leading-Edge Roughness for Transition Control on Swept-Wings," *AIAA 2000-0283*, 2000.

[22]Radeztzky, R.H., Reibert, M.S., Saric, W.S., Takagi, S., "Effect of Micron-Sized Roughness on Transition in Swept-Wing Flows," *AIAA 93 -0076*, 1993.

[23]Moes, T.R., Sarma, G.R., Mangalam, S.M., "Flight Demonstration of a Shock Location Sensor Using Constant Voltage Hotfilm Anemometry," *NASA TM 4806*, Aug. 1997.

[24]Mangalam, S.M., Maddalon, D.V., Saric, W.S., Agarwal, N.K., "Measurement of Crossflow Vortices, Attachment-Line Flow, and Transition Using Microthin Hotfilms, *AIAA 90-1636*, 1990.

[25]Agarwal, N.K., Maddalon, D.V., Mangalam, S.M., Collier, F.S., "Crossflow Vortex and Transition Measurements by Use of Multi-element Hotfilms," *AIAA J., Vol. 30, No. 9*, September 1992.

[26]Chapman, K.L., Glauser, M., Dagenhart, J.R., and Saric, W.S. "Application of Multipoint Correlation Techniques to Aerodynamic Flows," *AIAA Paper No. 94-2279*.

[27] Saric, W.S. "Boundary-Layer Stability and Transition." *Springer Handbook of Experimental Fluid Mechanics* Springer-Verlag Berlin Heidelberg, Ed: Cameron Tropea, Alexander Yarin, John F. Foss. Chapter C.12, Section 12.3 pp. 886-896, 2007

[28]Preston, J.H., "The Determination of Turbulent Skin Friction by Means of Pitot Tubes," *J. Roy. Aero. Soc. 58*, 1954.

[29]Patel, V.C., "Calibration of the Preston Tube and Limitations on Its Use in Pressure Gradients," *J. Fluid Mech.* 35(1), 1965.

[30]Bechert, D.W., "Calibration of Preston Tubes," *AIAA J., Vol. 34, No. 1, Pg 205 – 206*.

[31]Radeztsky, R.H., Reibert, M.S., Takagi, S., "A Software Solution to Temperature-Induced Hotwire Voltage Drift," *Proceedings of the Third International Symposium on Thermal Anemometry*, 1993.

[32]Sarma, G.R., Moes, T.R., "Demonstration of skin friction measurements featuring *in situ* estimation of conduction loss using constant voltage anemometers and surface hotfilms," *Rev. Sci. Instruments 76*, 2005.

[33]Bellhouse, B.J., Schultz, D.L., "Determination of mean and dynamic skin friction, separation and transition in low-speed flow with a thin-film heated element," *J.Fluid Mech., Vol 24, part 2, pages 379 – 400*, 1966.